



## An actin-based viscoplastic lock ensures progressive body-axis elongation

Alicia Lardennois, Teresa Ferraro, Flora Llense, Michel Labouesse, Gabriella Pásti, Julien Pontabry, David Rodriguez, Samantha Kim, Christelle Gally, Pierre Mahou, et al.

### ► To cite this version:

Alicia Lardennois, Teresa Ferraro, Flora Llense, Michel Labouesse, Gabriella Pásti, et al.. An actin-based viscoplastic lock ensures progressive body-axis elongation. *Nature*, 2019, 573 (7773), pp.266-270. 10.1038/s41586-019-1509-4 . hal-02372075

HAL Id: hal-02372075

<https://polytechnique.hal.science/hal-02372075>

Submitted on 17 Nov 2020

**HAL** is a multi-disciplinary open access archive for the deposit and dissemination of scientific research documents, whether they are published or not. The documents may come from teaching and research institutions in France or abroad, or from public or private research centers.

L'archive ouverte pluridisciplinaire **HAL**, est destinée au dépôt et à la diffusion de documents scientifiques de niveau recherche, publiés ou non, émanant des établissements d'enseignement et de recherche français ou étrangers, des laboratoires publics ou privés.

- 1
- 2 **An actin-based viscoplastic lock ensures progressive body**
- 3 **axis elongation**
- 4 Alicia Lardennois, Teresa Ferraro, Flora Llense & Michel  
Labouesse
- 5 CNRS UMR7622, Institut de Biologie Paris-Seine (IBPS), Sorbonne Université, Paris, France
- 6 Gabriella Pásti, Julien Pontabry, David Rodriguez, Samantha  
Kim, Christelle Gally & Michel Labouesse
- 7 IGBMC –CNRS UMR 7104, INSERM U964, Development and Stem Cells Department, Université de Strasbourg,  
Illkirch, France
- 8 Pierre Mahou & Emmanuel Beaurepaire
- 9 INSERM U1182 – CNRS/ UMR7645, Laboratoire d'Optique et Biosciences, Ecole Polytechnique, Paris, France
- 10 Julien Pontabry
- 11 RS2D, Mundolsheim, France
- 12 Shoichiro Ono
- 13 Departments of Pathology and Cell Biology, Winship Cancer Institute, Emory University School of Medicine,  
Atlanta, GA, USA
- 14
- 15
- 16
- 17
- 18
- 19
- 20 # Corresponding author: michel.labouesse@upmc.fr

21

22

23 **Abstract**

24

25

26 A key step in animal development is the process of body axis elongation, laying out the  
27 final form of the entire animal. This critically depends on polarized cell shape changes<sup>1</sup>,  
28 which rely on the interplay between intrinsic forces generated by molecular motors<sup>2-5</sup>,  
29 extrinsic forces due to adjacent cells pulling or pushing on the tissue<sup>6-9</sup>, and mechanical  
30 resistance forces due to cell and tissue elasticity or friction<sup>10-12</sup>. Understanding how  
31 mechanical forces influence morphogenesis at the cellular and molecular level remains  
32 a critical challenge<sup>2</sup>. Recent work outlined that cell shape changes occur through small  
33 incremental steps<sup>2,4,5,13</sup>, suggesting the existence of specific mechanisms to stabilize cell  
34 shapes and counteract cell elasticity. Here, we identify a spectrin-kinase-formin network  
35 required to stabilize embryo shape when repeated muscle contractions promote *C.*  
36 *elegans* embryo axis elongation. Its absence induces complete axis retraction due to  
37 damage of epidermal actin stress fibers. Modeling predicts that a mechanical  
38 viscoplastic deformation process can account for embryo shape stabilization. Molecular  
39 analysis suggests that the physical basis for viscoplasticity originates from the progressive  
40 shortening of epidermal microfilaments induced by muscle contractions and FHOD-1  
41 formin activity. Our work thus identifies an essential molecular lock acting in a  
42 developmental ratchet-like process.

43

44  
45  
46 *C. elegans* provides a simple and integrated model to study the cellular impact of  
47 mechanical forces. Its embryonic elongation only relies on cell shape changes and  
48 includes two phases depending on tension and stiffness anisotropies in the epidermis<sup>12</sup>,  
49 and beyond the 2-fold stage on muscle activity<sup>8</sup> (Fig. 1a; Supplementary material).  
50 Importantly, neither stage relies on pulsatile actomyosin flows<sup>12</sup>, as observed in the early  
51 *C. elegans* zygote, or during *Drosophila* gastrulation and germband extension<sup>2,4,5,13</sup>.  
52 Because muscles are tightly mechanically coupled to the epidermis through epidermal  
53 hemidesmosomes<sup>14</sup>, their contractions also displace the epidermis. This can be  
54 monitored by tracking the anterior-posterior displacement of muscle nuclei and the  
55 circumferentially oriented epidermal actin filaments (Fig. 1b-b''). Importantly, all  
56 muscles do not contract simultaneously (X. Yang and M. Labouesse, unpublished).  
57 Hence, when some areas of the epidermis are longitudinally compressed (red line in Fig.  
58 1c'), others are stretched (green line in Fig. 1c') before eventually relaxing (Fig. 1c-c";  
59 Fig. S1). Importantly, we previously established that the tension generated by muscle  
60 activity triggers a mechanotransduction pathway in the epidermis, which promotes axis  
61 elongation<sup>8</sup>.

62 The relaxation observed after each muscle contraction raises a conundrum: how can  
63 muscle activity power embryonic elongation from 100 µm to 200 µm within an hour if cell  
64 elasticity brings cells back to their initial length after each contraction (Fig. 1d). One  
65 simple hypothesis would be that some mechanism stabilizes the transient body  
66 deformations induced by muscle activity (Fig. 1d'), as was proposed for *Drosophila*  
67 gastrulation or germband extension in processes involving myosin II<sup>5,15,16</sup>. To uncover this  
68 mechanism, we focused on the kinase PAK-1, which lies at the crossroads of

69 hemidesmosome remodelling<sup>9</sup> and actomyosin force regulation<sup>17,18</sup>. We first performed  
70 a feeding RNAi screen in a strong yet viable *pak-1* mutant, looking for enhancers of  
71 embryonic lethality and/or body morphology defects (Fig. 2a). This screen identified the  
72 gene *spc-1* encoding  $\alpha$ -spectrin as a strong *pak-1* genetic enhancer leading to short  
73 hatchlings (58  $\mu\text{m}$  on average), which were significantly shorter than *pak-1(tm403)* (178  
74  $\mu\text{m}$ ) or *spc-1(RNAi)* (91  $\mu\text{m}$ ) hatchlings (Fig. 2b, Table S1). The study of this genetic  
75 interaction was further motivated by the identification of the central Src Homology 3  
76 domain (SH3) of SPC-1 as an interactor of the N-terminal domain of PAK-1 in a yeast  
77 two-hybrid screen (Fig. 2c, Table S2). Both screens thus point to an interaction between  
78 SPC-1 and PAK-1.

79 To understand why *pak-1(tm403)* *spc-1(RNAi)* are shorter than *spc-1(RNAi)* embryos, we  
80 examined their elongation rate using DIC microscopy. Wild-type and *pak-1(tm403)*  
81 embryos initially elongated at the same rate, whereas *spc-1* defective embryos  
82 elongated slower and stopped around the 2-fold stage (100  $\mu\text{m}$ ) as previously  
83 described<sup>19</sup> (Fig. 2d). By contrast, *spc-1(ra409)* *pak-1(tm403)* and *spc-1(RNAi)* *pak-*  
84 *1(tm403)* embryos reached  $\approx$ 65  $\mu\text{m}$  at a slow rate, but then could not maintain their  
85 shape, retracting back to  $\approx$ 50  $\mu\text{m}$ , which neither *spc-1(ra409)* nor *pak-1(tm403)* embryos  
86 did (Fig. 2d, Movie 1). Two observations suggest that this phenotype is linked to muscle  
87 activity. First, *spc-1* knock-down in *git-1* or *pix-1* mutants, two other players involved in  
88 the same mechanotransduction pathway as PAK-1<sup>9</sup>, also induced retraction (Fig. S2).  
89 Second, *spc-1(RNAi)* *pak-1(tm403)* embryos started to retract at the onset of active  
90 muscle contraction in control embryos (pink box in Fig. 2d). To directly prove this  
91 hypothesis, we abrogated muscle function in *spc-1(ra409)* *pak-1(tm403)* embryos by  
92 knocking-down the kindlin homolog UNC-112<sup>20</sup>. Strikingly, *spc-1(ra409)* *pak-1(tm403)*

93 embryos defective for *unc-112* no longer retracted (Fig. 2e; Movie 2). We conclude that  
94 the mechanical input provided by muscles to the epidermis induces the retraction  
95 phenotype observed in *spc-1 pak-1* double mutants.

96 The simplest interpretation of the retraction phenotype described above is that a  
97 cellular structure maintaining embryo shape fails to emerge or collapses in *spc-1 pak-1*  
98 double mutants once muscles become active. Two arguments lead us to consider that  
99 this structure corresponds to the actin cytoskeleton. First, SPC-1/α-spectrin and its  
100 binding partner SMA-1/β-spectrin form an actin-binding hetero-tetramer colocalizing  
101 with actin<sup>21</sup> and partially with PAK-1 in epidermal cells (Fig. S3). Second and foremost, it  
102 has long been known that treating *C. elegans* embryos with the actin-depolymerizing  
103 drug cytochalasin-D induces a retraction phenotype very similar to that presented  
104 herein<sup>22</sup>. We thus characterized actin filaments by spinning-disk confocal imaging of a  
105 LifeAct::GFP probe<sup>12</sup>. Segmentation analysis of the fluorescence signal associated with  
106 actin filaments in the dorso-ventral epidermis (Fig. 3a-a'') revealed more discontinuity in  
107 *spc-1 pak-1* double deficient embryos (Fig. 3d-d'') compared to the control genotypes  
108 (Fig. 3a-c''). Moreover, Fourier transform analysis indicated that their degree of  
109 anisotropy relative to the circumferential axis was abnormal (Fig. 3d''-d'''). Note that  
110 both phenotypes were visible mainly at mid elongation, i.e. after muscles become  
111 active (Fig. S4), suggesting that a well-structured actin network emerges too slowly in  
112 double mutants rather than it collapses.

113 Collectively, the results described so far, together with the retraction phenotype of  
114 cytochalasin-D treated embryos<sup>22</sup>, suggest that the actin filament defects account for  
115 *spc-1 pak-1* embryo retraction, and further link muscle activity with these defects.

116 Significantly, as the wild-type embryo lengthens, its circumference decreases by roughly  
117 20% due to embryo volume conservation (Fig. S5) and thus, the length of actin filaments  
118 in dorso-ventral cells should decrease. Hence, we suggest that muscle activity normally  
119 promotes actin filament shortening, probably through sliding or shortening of filaments  
120 relative to each other after their bending (Fig. S1). We further suggest that SPC-1 and  
121 PAK-1 stabilize cell shape by maintaining actin bundle integrity. We could not define the  
122 shortening mechanism by spinning-disk microscopy, probably because each muscle  
123 contraction results in changes beyond the time and space resolution of the microscope.  
124 However, we suggest that it goes awry in the absence of SPC-1 and PAK-1, due to the  
125 lack of a capping or bundling activity (Fig. 4b-b').

126 To rationalize the role of muscles in the process of actin bundle shortening and  
127 stabilization, we described the *C. elegans* embryo as a Kelvin-Voigt material (a spring in  
128 parallel to a dashpot) submitted to forces acting in the epidermis and muscles ( $F_{epid}$  and  
129  $F_{muscles}$ ) (Fig. 4c equations-a and -b; Supplementary material). Note that  $F_{epid}$  is written as  
130 the product of an active force,  $F_{seam}$ , and a passive component resulting from actin  
131 bundle stiffness,  $\alpha_{DV}$  (Supplementary material and ref. 11). Since muscle-defective  
132 mutants cannot elongate beyond the 2-fold stage, then  $F_{epid}$  can only extend embryos  
133 until that stage (due to the spring restoring force; Fig. S6a-a'). Simply adding the force  
134  $F_{muscles}$  should not trigger any further extension, because it oscillates between a positive  
135 and negative input (Fig. 1bc, Fig. S6b-b').

136 Recently, several studies have suggested that systems exposed to a stress can undergo  
137 a permanent rearrangement, which can be described as a plastic deformation<sup>23</sup> or as  
138 a change in the spring resting length<sup>24,25</sup>. Accordingly, we incorporated an increase of

139 the spring resting length  $\lambda$  in the equations described above by writing that it changes  
140 by a factor  $\beta$  (Fig. 4c equation-c; Fig. 4d). Thereby, we could accurately predict the  
141 elongation pattern of wild-type embryos (Fig. 4f, Fig. S6d-d'; Supplementary material).  
142 Conversely, in *spc-1 pak-1* defective embryos, the continuing damage to actin  
143 filaments should reduce their stiffness (component  $\alpha_{DV}$  in Fig. 4c equation-b), which we  
144 expressed by writing that it depends on a tearing factor  $\gamma$  (Fig. 4c equation-d, Fig. 4e);  
145 thereby, we could accurately predict their retraction pattern (Fig. 4f, Fig. S6e-e'). We  
146 thus propose that SPC-1/ $\alpha$ -spectrin and PAK-1 regulate a process of mechanical  
147 plasticity in the physical sense. From a cellular standpoint, having a changing resting  
148 length means that body elasticity does not bring the embryo back to its initial shape  
149 upon muscle relaxation, enabling progressive lengthening.

150 To further define the molecular basis of viscoplasticity, we performed a small-scale RNAi  
151 screen to search for gene knockdowns inducing retraction of *spc-1(ra409)* embryos (Fig.  
152 4g; Table S3). This screen identified the atypical formin FHOD-1 (Fig. 4h-i; Fig. S7, movie  
153 3), which has previously been linked to actin dynamics in the epidermis<sup>26</sup>. We confirmed  
154 that *fhod-1(tm2363); spc-1(RNAi)* embryos also showed a penetrant retraction  
155 phenotype (Fig. 4h; Fig. S7). The identification of this specific formin was intriguing  
156 because vertebrate FHOD1 promotes actin capping and bundling rather than  
157 nucleation and elongation<sup>27</sup>. It thus raised the tantalizing possibility that FHOD-1 activity  
158 stabilizes the actin cytoskeleton while it gets remodeled under the influence of muscle  
159 activity during embryo circumference reduction. Furthermore, the genetic interaction  
160 suggests that FHOD-1 acts with SPC-1 and PAK-1. To examine this possibility, we tested  
161 whether FHOD-1 derivatives removing at least the C-terminal DAD domain, predicted to  
162 auto-inhibit formins<sup>28</sup>, can rescue the retraction phenotype of *spc-1 pak-1* deficient

163 embryos. Strikingly, after epidermis-specific expression of a form lacking the FH2 and  
164 DAD domains, transgenic *spc-1(RNAi)* *pak-1(tm403)* embryos did not retract and were  
165 significantly longer than non-transgenic siblings; rescue was better than with the full-  
166 length protein. By contrast, the DAD deleted form did not rescue and deletion of the  
167 FH1-FH2-DAD domains marginally rescued retraction, arguing that the FH2 F-actin  
168 nucleation domain is not necessary for rescue but that the FH1 is. Truncation of the C-  
169 terminal DAD domain or of the FH1-FH2-DAD domains marginally rescued retraction (Fig.  
170 4j). Importantly, an FH2-DAD truncation in the mammalian FHOD1 still enables it to  
171 bundle actin<sup>27</sup>, further strengthening the notion that FHOD-1 bundling activity is indeed  
172 required and providing a potential molecular basis for viscoplasticity. It also indicates  
173 that muscle-induced actin remodeling would primarily result from sliding and re-  
174 bundling (see Fig. 4a-a'). Furthermore, we conclude that the retraction of *spc-1 pak-1*  
175 deficient embryos mainly results from a lack of FHOD-1 activation.

176 Several factors could contribute to improperly regulate the activity of PAK-1 and FHOD-  
177 1. First, SPC-1 could help recruit FHOD-1 and PAK-1, since FHOD-1::GFP and PAK-1::GFP  
178 made small aggregates in SPC-1 defective embryos (Fig. S8). Second, we found that  
179 the cycles of actin filament displacement induced by muscle contractions were almost  
180 twice as short in *spc-1(RNAi)* *pak-1(tm403)* embryos compared to *pak-1(tm403)* and  
181 wild-type controls (3 sec against 5.7 sec; Fig. S9, Movie 4). These shorter muscle  
182 contractions might still induce actin filament shortening but not give enough time for  
183 their stabilization. Third, PAK-1 might directly activate FHOD-1 downstream of the  
184 mechanotransduction pathway induced by muscles, since *git-1* and *pix-1* mutations  
185 combined with *spc-1* RNAi-knockdown also induced a retraction (see Fig. S2a-g).

186 Altogether, our data identify three proteins involved in stabilizing cell shapes in a system  
187 involving two mechanically interacting tissues submitted to repeated stress. We propose  
188 that the progressive shortening of actin filaments under the control of these factors  
189 mediates a cellular viscoplastic process promoting axis elongation. A similar  
190 spectrin/p21-activated kinase/FHOD1 system might operate in vertebrate tissues  
191 comprising an epithelial layer surrounded by a contractile layer, such as our internal  
192 organs. Interestingly, high FHOD1 expression correlates with poor prognosis of breast  
193 cancer patients<sup>29</sup>. Thus, a similar viscoplastic process might also influence the metastatic  
194 properties of tumor cells positioned next to contractile cells.

195

## 196 **ACKNOWLEDGEMENTS**

197 The authors thank Anne Spang, Stephan Grill, Yohanns Bellaïche for critical comments  
198 on the manuscript, and Melanie Gettings for improving the English. We also thank the  
199 *Caenorhabditis* Genetics Center (funded by the NIH Office of Research Infrastructure  
200 Programs P40 OD010440) for strains, and the IBPS Imaging Facility for advice. This work  
201 was supported by an Agence Nationale pour la Recherche, European Research  
202 Council (grant #294744), Israël-France Maïmonide exchange program grants, and  
203 installation funds from the Centre National de la Recherche Scientifique (CNRS) and  
204 University Pierre et Marie Curie (UPMC) to ML. This work was also made possible by  
205 institutional funds from the CNRS, University of Strasbourg and UPMC, the grant ANR-10-  
206 LABX-0030-INRT which is a French State fund managed by the Agence Nationale de la  
207 Recherche under the framework programme Investissements d'Avenir labelled ANR-10-  
208 IDEX-0002-02 to the IGBMC.

209

210 **AUTHORS' CONTRIBUTIONS**

211 ML conceived the project, GP initiated many aspects of the study while AL performed  
212 most experiments, with contributions from TF for modelling, TF and JP for image analysis,  
213 FL for the generation of FHOD-1 variants, CG shared data from a related screen, SK for  
214 the *spc-1(ra409)* mini-RNAi screen, DR for technical assistance. ML wrote the manuscript  
215 and all authors commented and proofread it (except SK, who was an intern), AL  
216 assembled figures, TF wrote the Supplementary mathematical modelling material, and  
217 FL the Materials section.

218

219

220

221 **FIGURE LEGENDS**

222 **Figure 1: Muscle contractions deform the epidermis to their mechanical coupling**

223 **(a)** *C. elegans* embryonic elongation from comma to 2-fold stages depends on a  
224 ROCK-promoted actomyosin force in seam cells (cyan) and actin-promoted stiffness in  
225 dorso-ventral cells (orange); elongation beyond the 2-fold stage requires repeated  
226 muscle contractions (red flash), which induce a PAK-1-dependent mechano-  
227 transduction pathway. Open cross-sections (bottom) show muscle positions. **(b-b'')**  
228 Epidermis actin filament (green) and muscle nucleus (red) tracking in a wild-type 2-fold  
229 embryo. **(b')** Kymographs from the yellow rectangle area **(b)** showing the concurrent

displacement of epidermal actin and muscle nuclei. **(b'')** Resulting displacement curves; **(b''')** quantification of the area between them; its low value underlines the tight mechanical coupling between both tissues. Scale bar, 10  $\mu$ m. **(c-c'')** A muscle contraction/relaxation cycle illustrating its local impact on epidermal actin filaments in a wild-type 2-fold embryo (timing in left corner). Yellow (relaxation), red (compression) green (stretching) distances between landmarks denoted 1-4: **(c)** [1-2], 7.8  $\mu$ m; [2-3], 19.8  $\mu$ m; [3-4], 24.6  $\mu$ m. **(c')** [1-2], 9.4  $\mu$ m; [2-3], 13.6  $\mu$ m; [3-4], 26.2  $\mu$ m. **(c'')** [1-2], 8.0  $\mu$ m; [2-3], 19.2  $\mu$ m; [3-4], 25.0  $\mu$ m. In **(b-c)** the *Pepidermis* promoter is *Pdpy-7*. **(d)** Hysteresis graph of an idealized elastic material returning to its initial shape after deformation (top), or showing permanent deformation<sup>30</sup> (bottom).

**Figure 2: Loss of PAK-1 and SPC-1 triggers a muscle-dependent retraction of embryos**

**(a)** RNAi screen in a *pak-1* mutant identified *spc-1* as an enhancer (Table S1). **(b)** DIC micrographs of newly hatched wild-type, *pak-1(tm403)* (scale bar: 10  $\mu$ m), *spc-1(RNAi)* and *spc-1(RNAi)* *pak-1(tm403)* (scale bar: 25  $\mu$ m). Quantification of L1 hatchling body length: wild-type (n=38); *pak-1(tm403)* (n=32); *spc-1(RNAi)* (n=26); *spc-1(RNAi)* *pak-1(tm40)* (n=36). **(c)** A yeast two-hybrid screen using the PAK-1 N-term domain as a bait identified the SPC-1 SH3 domain as a prey (orange background) (Table S2). **(d)** Elongation profiles and corresponding terminal phenotypes of wild-type (n=5), *pak-1(tm403)* (n= 5), *spc-1(RNAi)* (n=8), *spc(RNAi)* *pak-1(tm403)* (n=8). **(e)** Elongation profiles in a muscle defective background. *unc-112(RNAi)* (n=5); *spc-1(RNAi)* (n=8); *unc-112(RNAi)*; *pak-1(tm403)* *spc-1(ra409)* (n=5); *spc-1(RNAi)* *pak-1(tm403)* (n=8). Right bracket **(d, e)**, extent of retraction for *spc-1(RNAi)* *pak-1(tm403)* embryos. Scale bars, 10  $\mu$ m. Error bars, SEM.

254

255 **Figure 3: Actin filament defects in SPC-1 and PAK-1 defective embryos**

256 **(a-d)** Epidermal actin filaments visualized with the *Pdpy-7::LifeAct::GFP* reporter  
257 construct in wild-type **(a-a'')**, *pak-1(tm403)* **(b-b'')**, *spc-1(RNAi)* **(c-c'')** and *spc-1(RNAi)*  
258 *pak-1(tm403)* **(d-d'')** embryos at mid-elongation (2-fold equivalent) stage. Yellow  
259 rectangle, region of interest (ROI). Scale bar, 10  $\mu\text{m}$ . **(a'-d')** ROI after binarisation (green)  
260 and major axis detection (red), based on **(a'')** three steps of image treatment for  
261 continuity and orientation analysis. **(a''-d'')** Actin continuity: distribution of actin  
262 segments based on their length. Wild-type (n=16); *pak-1(tm403)* (n=21); *spc-*  
263 *1(RNAi)* (n=21) ; *spc-1(RNAi)* *pak-1(tm403)* (n=17) **(b'''-d'''')** Actin filament orientation:  
264 the curves represent the number of actin filaments oriented perpendicular to the  
265 elongation axis (90° angle in wild-type) based on the Fast Fourier Transformation (FFT in  
266 a''). Wild type (n=18) ; *pak-1(tm403)* (n=20) ; *spc-1(RNAi)* (n=18) ; *spc-1(RNAi)* *pak-*  
267 *1(tm403)* (n=18). Scale bars, 10  $\mu\text{m}$  (c, d, e, f), or 1  $\mu\text{m}$  (c', d', e', f'). P values, \* $<0,05$ ;  
268 \*\* $<0,001$ ; \*\*\* $<0,0001$ ; ns not significant.

269

270 **Figure 4: An actin-remodeling network providing mechanical plasticity ensures embryo**  
271 **elongation**

272 **(a-b')** Cellular model of embryo elongation. **(a-a')** In control embryos, muscle  
273 contractions (red arrows) provoke actin filament shortening in the dorso-ventral  
274 epidermis, probably through sliding or shortening, followed by SPC-1/PAK-1-dependent  
275 actin stabilization. Whether spectrin is found along (scenario 1) or between (scenario 2)  
276 actin filaments is unknown **(a)**. **(b-b')** In *spc-1* *pak-1* deficient embryos, actin remodeling  
277 goes uncontrolled. **(c-f)** Viscoplastic mechanical model of embryo elongation. The  
278 embryo is represented as a Kelvin-Voigt solid (spring stiffness  $k$ , resting length  $\lambda$ , viscosity

279 η) submitted to the forces  $F_{epid}$  and  $F_{muscle}$ . System equations for the model. **(d)** Wild-type  
280 case: an increasing resting length during stretching phases imparts mechanical  
281 plasticity. **(e)** *spc-1 pak-1* mutants:  $F_{epid}$  progressively decreases. **(f)** Comparison of  
282 experimental and predicted elongation curves taking the constitutive equations shown  
283 in **(c)**. **(g)** A retraction screen in a *spc-1* mutant identifies *fhod-1*. **(h)** Snapshot at three  
284 time-points of *spc-1* deficient embryos in control, *pak-1* or *fhod-1* backgrounds; **(i)**  
285 terminal body length at hatching: *spc-1(ra409)* after feeding on L4440 control (n=21), or  
286 *fhod-1(RNAi)* (n=25) bacteria. **(j)** *Pdpy-7* driven epidermis expression of truncated FHOD-  
287 1 variants and terminal body length at hatching: *spc-1(RNAi)* (n=26); *spc-1(RNAi)pak-1(tm403)* no transgene (n=36), FHOD-1(full length) (n=16), FHOD-1(ΔDAD) (n=17), FHOD-  
288 1(ΔFH2-DAD) (n=38) and non-transgenic siblings (n=78), FHOD-1(ΔFH1-FH2-DAD) (n=18).  
289 Scale bar, 15 μm. Error bars, SEM. P values: \* $<0,05$ ; \*\* $<0,001$ ; \*\*\* $<0,0001$ ; ns, not significant.  
290

291  
292  
293

**References**

- 297 1 Tada, M. & Heisenberg, C. P. Convergent extension: using collective cell  
298 migration and cell intercalation to shape embryos. *Development* **139**,  
299 3897-3904, doi:10.1242/dev.073007 (2012).
- 300 2 Gilmour, D., Rembold, M. & Leptin, M. From morphogen to morphogenesis  
301 and back. *Nature* **541**, 311-320, doi:10.1038/nature21348 (2017).
- 302 3 Keller, R. Developmental biology. Physical biology returns to  
303 morphogenesis. *Science* **338**, 201-203, doi:10.1126/science.1230718 (2012).
- 304 4 Martin, A. C., Kaschube, M. & Wieschaus, E. F. Pulsed contractions of an  
305 actin-myosin network drive apical constriction. *Nature* **457**, 495-499,  
306 doi:nature07522 [pii]  
307 10.1038/nature07522 (2009).
- 308 5 Rauzi, M., Lenne, P. F. & Lecuit, T. Planar polarized actomyosin contractile  
309 flows control epithelial junction remodelling. *Nature* **468**, 1110-1114,  
310 doi:nature09566 [pii]  
311 10.1038/nature09566 (2010).
- 312 6 Collinet, C., Rauzi, M., Lenne, P. F. & Lecuit, T. Local and tissue-scale forces  
313 drive oriented junction growth during tissue extension. *Nat Cell Biol* **17**,  
314 1247-1258, doi:10.1038/ncb3226 (2015).
- 315 7 Desprat, N., Supatto, W., Pouille, P. A., Beaurepaire, E. & Farge, E. Tissue  
316 deformation modulates twist expression to determine anterior midgut  
317 differentiation in *Drosophila* embryos. *Dev Cell* **15**, 470-477,  
318 doi:10.1016/j.devcel.2008.07.009 (2008).
- 319 8 Lye, C. M. et al. Mechanical Coupling between Endoderm Invagination  
320 and Axis Extension in *Drosophila*. *PLoS Biol* **13**, e1002292,  
321 doi:10.1371/journal.pbio.1002292 (2015).
- 322 9 Zhang, H. et al. A tension-induced mechanotransduction pathway  
323 promotes epithelial morphogenesis. *Nature* **471**, 99–103,  
324 doi:10.1038/nature09765 (2011).
- 325 10 Behrndt, M. et al. Forces driving epithelial spreading in zebrafish  
326 gastrulation. *Science* **338**, 257-260, doi:10.1126/science.1224143 (2012).
- 327 11 Dierkes, K., Sumi, A., Solon, J. & Salbreux, G. Spontaneous oscillations of  
328 elastic contractile materials with turnover. *Phys Rev Lett* **113**, 148102,  
329 doi:10.1103/PhysRevLett.113.148102 (2014).
- 330 12 Vuong-Breder, T. T., Ben Amar, M., Pontabry, J. & Labouesse, M. The  
331 interplay of stiffness and force anisotropies drive embryo elongation. *eLife*  
332 **6**, doi:10.7554/eLife.23866 (2017).
- 333 13 Munro, E., Nance, J. & Priess, J. R. Cortical flows powered by asymmetrical  
334 contraction transport PAR proteins to establish and maintain anterior-

- 335 posterior polarity in the early *C. elegans* embryo. *Developmental cell* **7**,  
336 413-424, doi:10.1016/j.devcel.2004.08.001 (2004).
- 337 14 Vuong-Bender, T. T., Yang, X. & Labouesse, M. C. *elegans* Embryonic  
338 Morphogenesis. *Curr Top Dev Biol* **116**, 597-616,  
339 doi:10.1016/bs.ctdb.2015.11.012 (2016).
- 340 15 Simoes Sde, M., Mainieri, A. & Zallen, J. A. Rho GTPase and Shroom direct  
341 planar polarized actomyosin contractility during convergent extension.  
342 *The Journal of cell biology* **204**, 575-589, doi:10.1083/jcb.201307070 (2014).
- 343 16 Vasquez, C. G., Tworoger, M. & Martin, A. C. Dynamic myosin  
344 phosphorylation regulates contractile pulses and tissue integrity during  
345 epithelial morphogenesis. *The Journal of cell biology* **206**, 435-450,  
346 doi:10.1083/jcb.201402004 (2014).
- 347 17 Gally, C. et al. Myosin II regulation during *C. elegans* embryonic  
348 elongation: LET-502/ROCK, MRCK-1 and PAK-1, three kinases with different  
349 roles. *Development* **136**, 3109-3119, doi:10.1242/dev.039412 (2009).
- 350 18 Vuong-Bender, T. T. K., Suman, S. K. & Labouesse, M. The apical ECM  
351 preserves embryonic integrity and distributes mechanical stress during  
352 morphogenesis. *Development*, doi:10.1242/dev.150383 (2017).
- 353 19 Norman, K. R. & Moerman, D. G. Alpha spectrin is essential for  
354 morphogenesis and body wall muscle formation in *Caenorhabditis*  
355 *elegans*. *The Journal of cell biology* **157**, 665-677,  
356 doi:10.1083/jcb.200111051 (2002).
- 357 20 Rogalski, T. M., Mullen, G. P., Gilbert, M. M., Williams, B. D. & Moerman, D.  
358 G. The UNC-112 gene in *Caenorhabditis elegans* encodes a novel  
359 component of cell-matrix adhesion structures required for integrin  
360 localization in the muscle cell membrane. *The Journal of cell biology* **150**,  
361 253-264 (2000).
- 362 21 Praitis, V., Ciccone, E. & Austin, J. SMA-1 spectrin has essential roles in  
363 epithelial cell sheet morphogenesis in *C. elegans*. *Dev Biol* **283**, 157-170  
364 (2005).
- 365 22 Priess, J. R. & Hirsh, D. I. *Caenorhabditis elegans* morphogenesis: the role of  
366 the cytoskeleton in elongation of the embryo. *Dev Biol* **117**, 156-173 (1986).
- 367 23 Bonakdar, N. et al. Mechanical plasticity of cells. *Nat Mater* **15**, 1090-1094,  
368 doi:10.1038/nmat4689 (2016).
- 369 24 Dubrovinski, K., Swan, M., Polyakov, O. & Wieschaus, E. F. Measurement of  
370 cortical elasticity in *Drosophila melanogaster* embryos using ferrofluids.  
371 *Proc Natl Acad Sci U S A* **114**, 1051-1056, doi:10.1073/pnas.1616659114  
372 (2017).
- 373 25 Munoz, J. J. & Albo, S. Physiology-based model of cell viscoelasticity. *Phys  
374 Rev E Stat Nonlin Soft Matter Phys* **88**, 012708,  
375 doi:10.1103/PhysRevE.88.012708 (2013).
- 376 26 Vanneste, C. A., Pruyne, D. & Mains, P. E. The role of the formin gene fmod-  
377 1 in *C. elegans* embryonic morphogenesis. *Worm* **2**, e25040,  
378 doi:10.4161/worm.25040 (2013).

- 379 27 Schonichen, A. et al. FHOD1 is a combined actin filament capping and  
380 bundling factor that selectively associates with actin arcs and stress fibers.  
381 *J Cell Sci* **126**, 1891-1901, doi:10.1242/jcs.126706 (2013).
- 382 28 Kuhn, S. & Geyer, M. Formins as effector proteins of Rho GTPases. *Small*  
383 *GTPases* **5**, e29513, doi:10.4161/sgtp.29513 (2014).
- 384 29 Jurmeister, S. et al. MicroRNA-200c represses migration and invasion of  
385 breast cancer cells by targeting actin-regulatory proteins FHOD1 and  
386 PPM1F. *Mol Cell Biol* **32**, 633-651, doi:10.1128/MCB.06212-11 (2012).
- 387 30 Vincent, J. in *Structural Biomaterials: Third Edition* 1-28 (Princeton  
388 University Press, 2012).
- 389
- 390
- 391

392

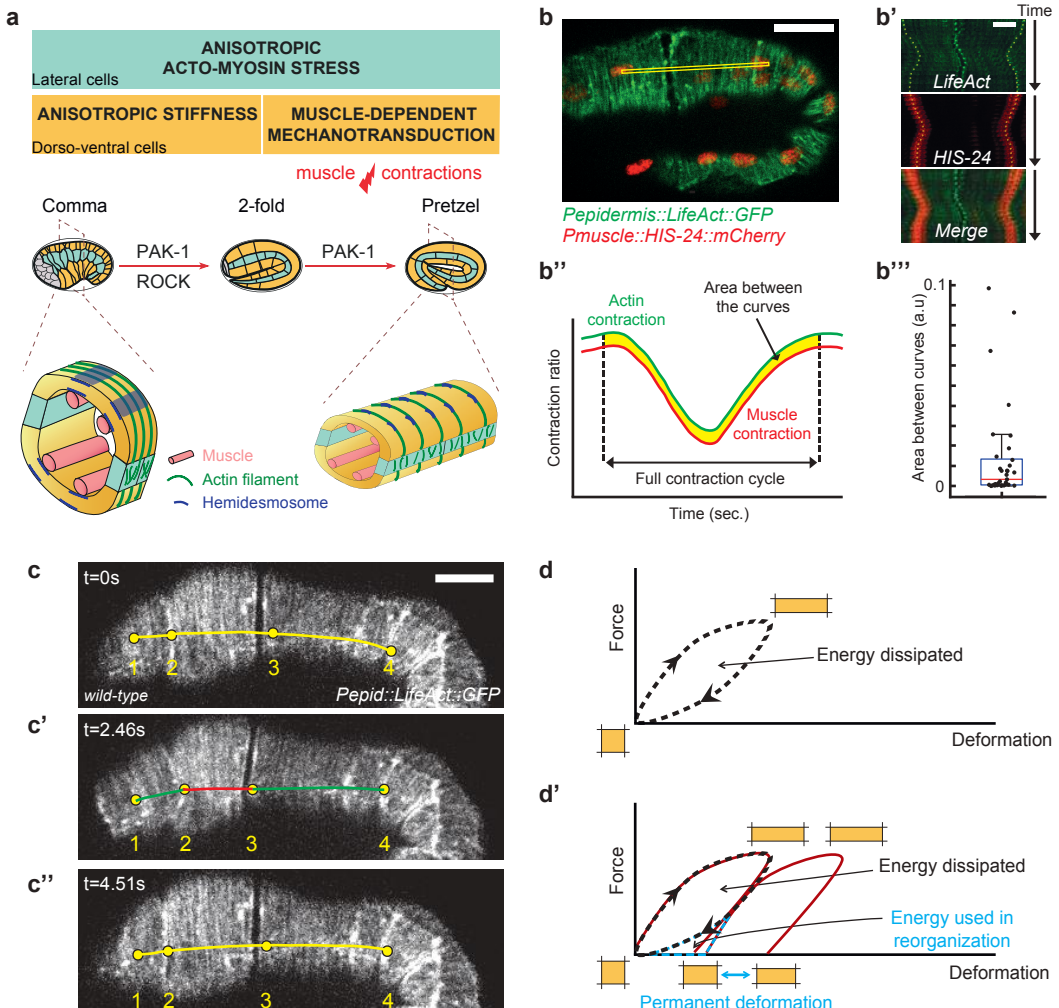


**Figure 1:** Muscle contractions deform the epidermis to their mechanical coupling

- (a) *C. elegans* embryonic elongation from comma to 2-fold stages depends on a ROCK-promoted actomyosin force in seam cells (cyan) and actin-promoted stiffness in dorso-ventral cells (orange); elongation beyond the 2-fold stage requires repeated muscle contractions (red flash), which induce a PAK-1-dependent mechano-transduction pathway. Open cross-sections (bottom) show muscle positions.
- (b) Kymographs from the yellow rectangle area (b) showing the concurrent displacement of epidermal actin and muscle nuclei.
- (b'') Resulting displacement curves;
- (b''') quantification of the area between them; its low value underlines the tight mechanical coupling between both tissues. Scale bar, 10  $\mu$ m.
- (c-c'') A muscle contraction/relaxation cycle illustrating its local impact on epidermal actin filaments in a wild-type 2-fold embryo (timing in left corner). Yellow (relaxation), red (compression) green (stretching) distances between landmarks denoted 1-4:
- (c) [1-2], 7.8  $\mu$ m; [2-3], 19.8  $\mu$ m; [3-4], 24.6  $\mu$ m.
- (c') [1-2], 9.4  $\mu$ m; [2-3], 13.6  $\mu$ m; [3-4], 26.2  $\mu$ m.
- (c'') [1-2], 8.0  $\mu$ m; [2-3], 19.2  $\mu$ m; [3-4], 25.0  $\mu$ m.
- In (b-c) the Pepid promoter is *Pdpy-7*.
- (d) Hysteresis graph of an idealized elastic material returning to its initial shape after deformation (top), or showing permanent deformation (bottom).

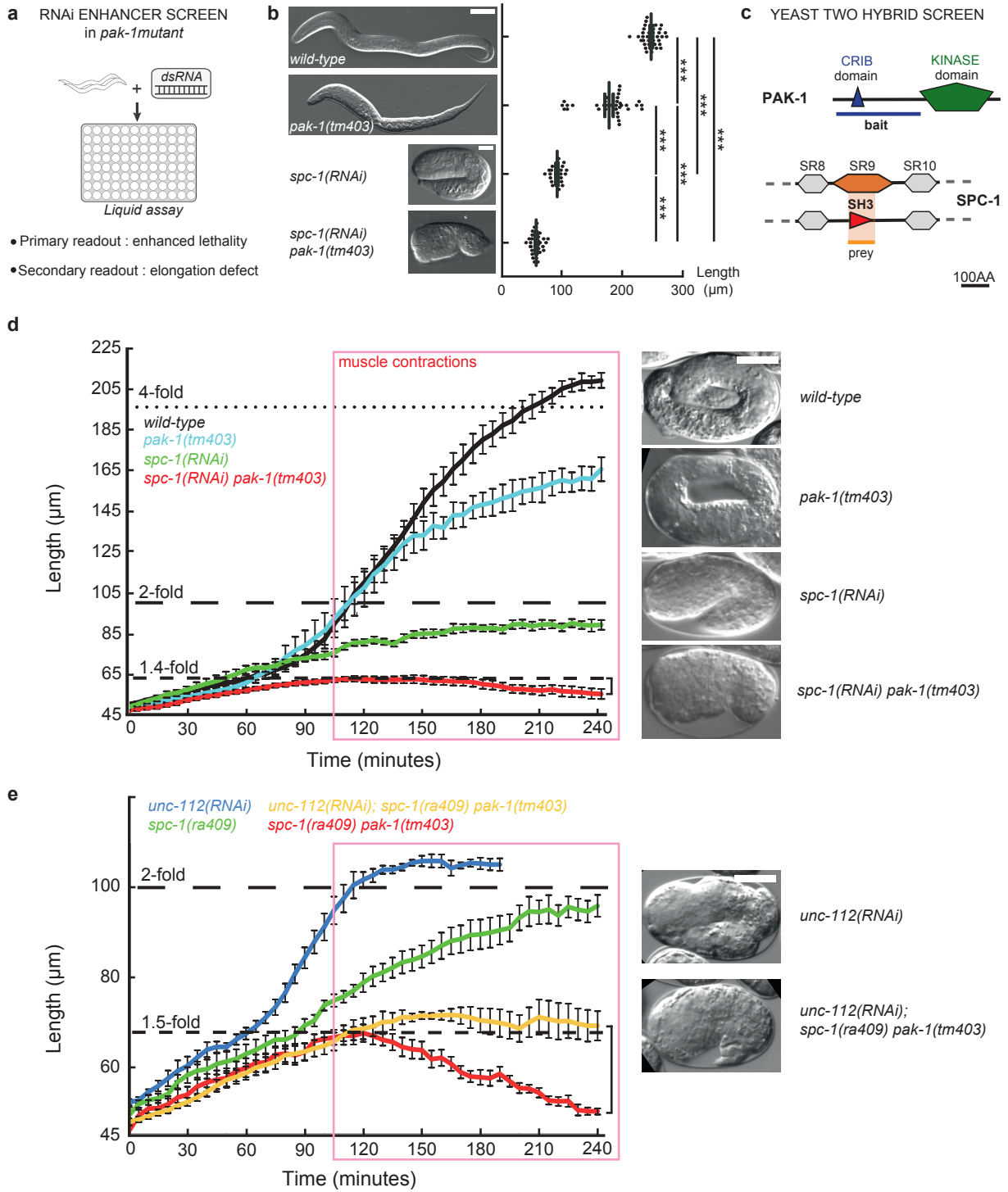


**Figure 2: Loss of PAK-1 and SPC-1 triggers a muscle-dependent retraction of embryos**

- (a) RNAi screen in a *pak-1* mutant identified *spc-1* as an enhancer (Table S1).  
 (b) DIC micrographs of newly hatched wild-type, *pak-1(tm403)* (scale bar: 10 μm), *spc-1(RNAi)* and *spc-1(RNAi)* *pak-1(tm403)* (scale bar: 25 μm). Quantification of L1 hatchling body length: wild-type (n=38); *pak-1(tm403)* (n=32); *spc-1(RNAi)* (n=26); *spc-1(RNAi)* *pak-1(tm403)* (n=36).  
 (c) A yeast two-hybrid screen using the PAK-1 N-term domain as a bait identified the SPC-1 SH3 domain as a prey (orange background) (Table S2).  
 (d) Elongation profiles and corresponding terminal phenotypes of wild-type (n=5), *pak-1(tm403)* (n= 5), *spc-1(RNAi)* (n=8), *spc-1(RNAi)* *pak-1(tm403)* (n=8).  
 (e) Elongation profiles in a muscle defective background.  
*unc-112(RNAi)* (n=5); *spc-1(RNAi)* (n=8); *unc-112(RNAi)*; *pak-1(tm403)* *spc-1(ra409)* (n=5); *spc-1(RNAi)* *pak-1(tm403)* (n=8). Right bracket (d, e), extent of retraction for *spc-1(RNAi)* *pak-1(tm403)* embryos. Scale bars, 10 μm. Error bars, SEM.

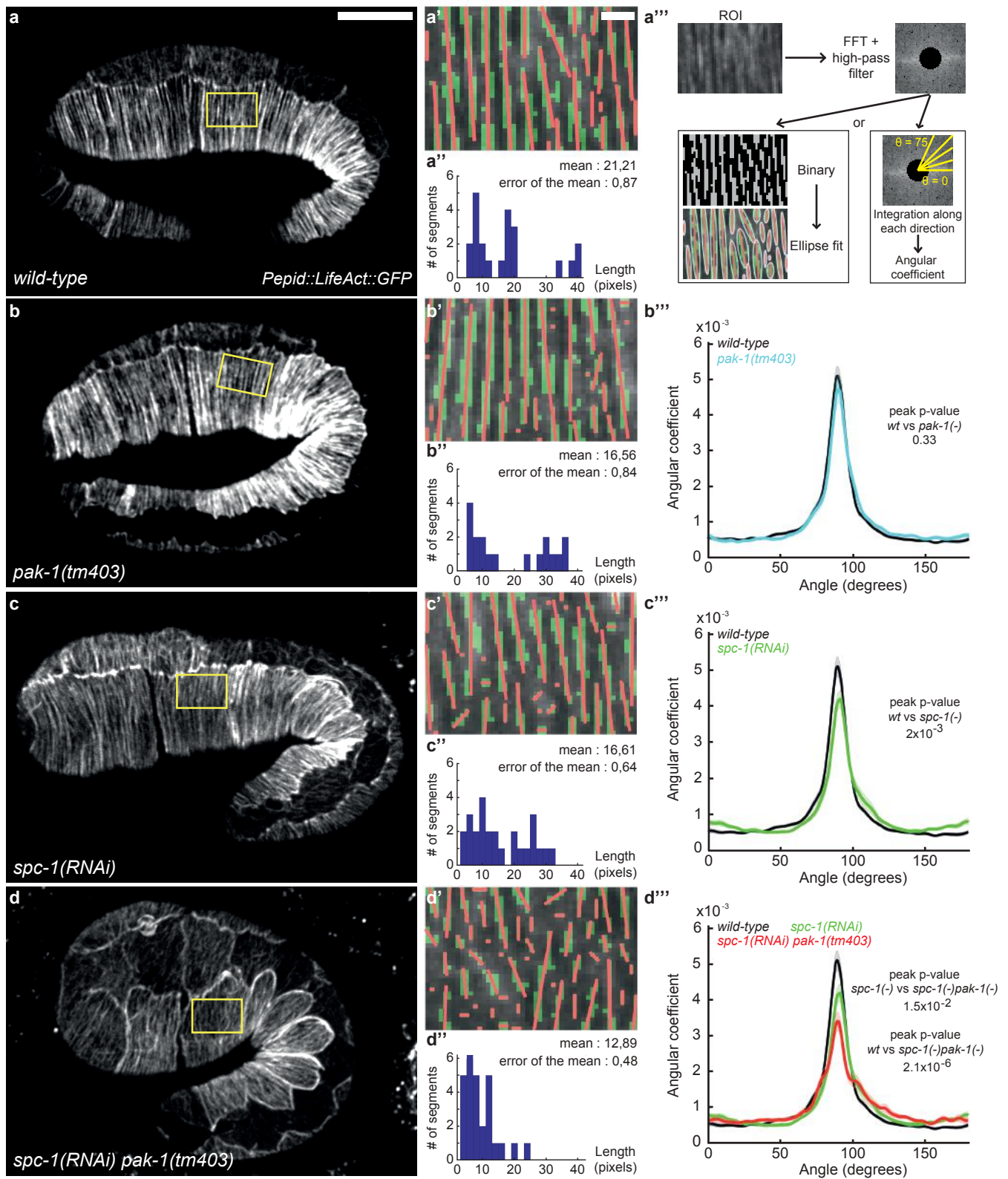


**Figure 3:** Actin filament defects in SPC-1 and PAK-1 defective embryos

(a-d) Epidermal actin filaments visualized with the Pdp7::LifeAct::GFP reporter construct in wild-type (a-a'''), pak-1(tm403) (b-b'''), spc-1(RNAi) (c-c''') and spc-1(RNAi) pak-1(tm403) (d-d''') embryos at mid-elongation (2-fold equivalent) stage. Yellow rectangle, region of interest (ROI). Scale bar, 10  $\mu$ m.

(a'-d') ROI after binarisation (green) and major axis detection (red), based on (a'') three steps of image treatment for continuity and orientation analysis.

(a''-d'') Actin continuity: distribution of actin segments based on their length. Wild-type (n=16); pak-1(tm403) (n=21); spc-1(RNAi) (n=21); spc-1(RNAi) pak-1(tm403) (n=17) (b''-d'') Actin filament orientation: the curves represent the number of actin filaments oriented perpendicular to the elongation axis (90° angle in wild-type) based on the Fast Fourier Transformation (FFT in a'').

Wild type (n=18); pak-1(tm403) (n=20); spc-1(RNAi) (n=18); spc-1(RNAi) pak-1(tm403) (n=18).

Scale bars, 10  $\mu$ m (c, d, e, f), or 1  $\mu$ m (c', d', e', f'). P values, \* $<0,05$ ; \*\* $<0,001$ ; \*\*\* $<0,0001$ ; ns not significant.

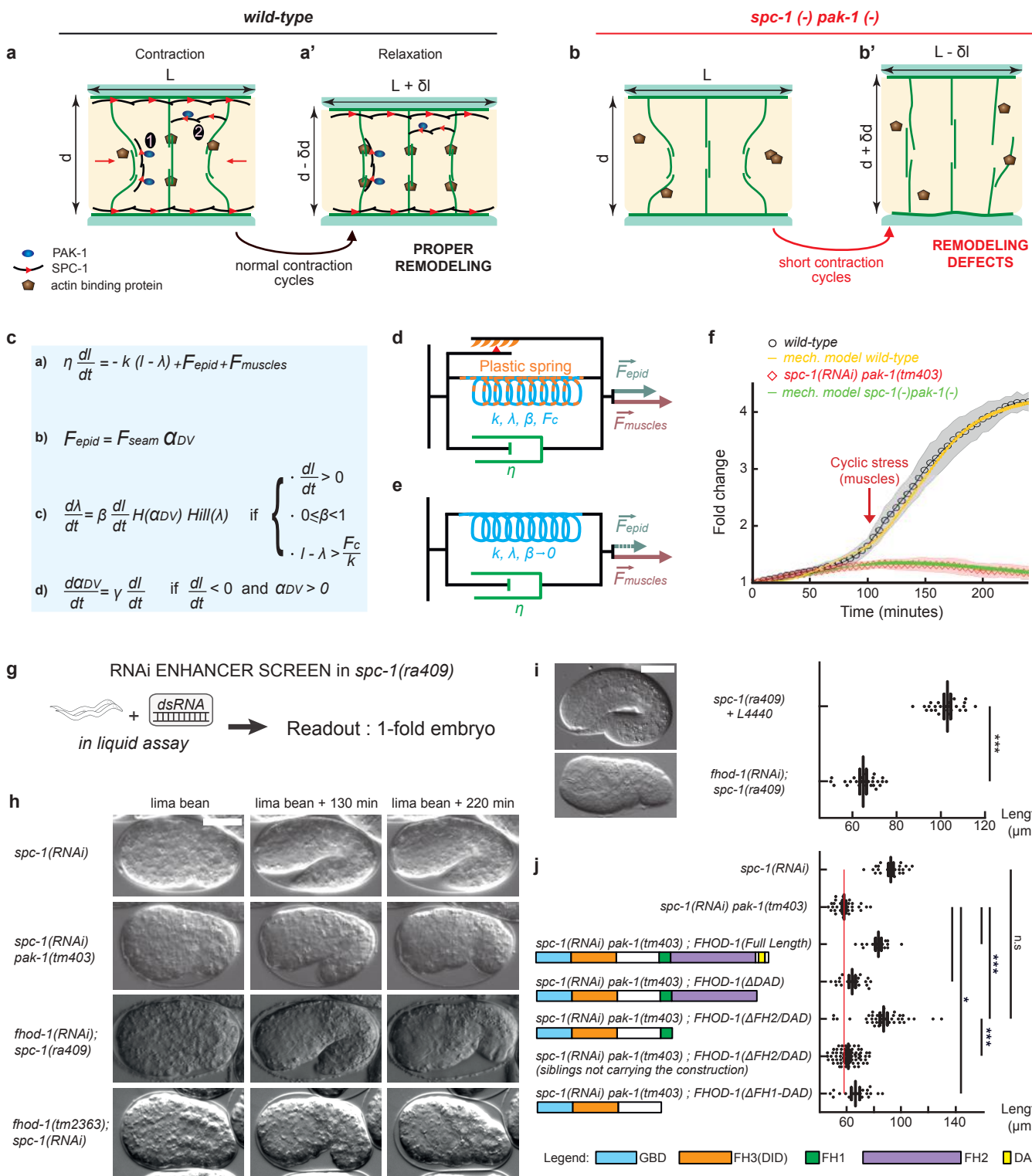


**Figure 4:** An actin-remodeling network providing mechanical plasticity ensures embryo elongation

(a-b') Cellular model of embryo elongation.

(a-a') In control embryos, muscle contractions (red arrows) provoke actin filament shortening in the dorso-ventral epidermis, probably through sliding or shortening, followed by SPC-1/PAK-1-dependent actin stabilization. Whether spectrin is found along (scenario 1) or between (scenario 2) actin filaments is unknown (a). (b-b') In *spc-1* *pak-1* deficient embryos, actin remodeling goes uncontrolled. (c-f) Viscoplastic mechanical model of embryo elongation. The embryo is represented as a Kelvin-Voigt solid (spring stiffness  $k$ , resting length  $\lambda$ , viscosity  $\eta$ ) submitted to the forces  $F_{epid}$  and  $F_{muscles}$ . System equations for the model. (d) Wild-type case: an increasing resting length during stretching phases imparts mechanical plasticity. (e) *spc-1* *pak-1* mutants:  $F_{epid}$  progressively decreases. (f) Comparison of experimental and predicted elongation curves taking the constitutive equations shown in (c).

(g) A retraction screen in a *spc-1* mutant identifies *fhod-1*.

(h) Snapshot at three time-points of *spc-1* deficient embryos in control, *pak-1* or *fhod-1* backgrounds;

(i) terminal body length at hatching: *spc-1(ra409)* after feeding on L4440 control ( $n=21$ ), or *fhod-1(RNAi)* ( $n=25$ ) bacteria. (j) Pdpy-7 driven epidermis expression of truncated FHOD-1 variants and terminal body length at hatching: *spc-1(RNAi)* ( $n=26$ ); *spc-1(RNAi)**pak-1(tm403)* no transgene ( $n=36$ ), FHOD-1(full length) ( $n=16$ ), FHOD-1( $\Delta$ DAD) ( $n=17$ ), FHOD-1( $\Delta$ FH2-DAD) ( $n=38$ ) and non-transgenic siblings ( $n=78$ ), FHOD-1( $\Delta$ FH1-FH2-DAD) ( $n=18$ ). Scale bar, 15 μm. Error bars, SEM. P values: \* $<0,05$ ; \*\* $<0,001$ ; \*\*\* $<0,0001$ ; ns, not significant.

1

## SUPPLEMENTARY MATERIAL

### 2 An actin-based viscoplastic lock ensures progressive body axis elongation

3 Alicia Lardennois<sup>1\*</sup>, Gabriella Pásti<sup>2\*</sup>, Teresa Ferraro<sup>1</sup>, Julien Pontabry<sup>2,3</sup>, David  
4 Rodriguez<sup>2</sup>, Samantha Kim<sup>2</sup>, Flora Llense<sup>1</sup>, Christelle Gally<sup>2</sup>, Michel Labouesse<sup>1,2</sup> #

5

### 6 Content

- 7 1- Supplementary Mechanical Modeling
- 8 2- Methods
- 9 3- Supplementary Figures S1-S8 with legends
- 10 4- Captions for movies S1-S8
- 11 5- Supplementary References

12

13

### 14 1-Supplementary Mechanical Modeling

15 **1.1 Background information.** During embryogenesis the *C. elegans* embryo  
16 undergoes a process of elongation whereby it becomes four times as long as the  
17 long axis of the eggshell (50 µm). Cell proliferation and cell intercalation are absent,  
18 therefore the process of axis elongation relies only on the ability of the embryo to  
19 extend in the anterior-posterior direction. The outer epithelium (epidermis) plays an  
20 essential role in this process.

21 Changing the status of any physical entity requires the involvement of a force  
22 (mechanical or chemical), and the *C. elegans* embryo is no exception to this rule of  
23 physics. During the first phase of elongation and until muscles become active, the

24 machinery driving elongation involves an active force in the lateral epidermis (also  
25 called seam cells), and a passive force exerted by the dorsal and ventral epidermal  
26 cells (called DV cells) adjacent to the seam cells (Fig. 1a). Seam cells have a high  
27 concentration of non-muscle myosin II, which has a non-polarized distribution and  
28 does not display pulsatile flows<sup>1,2</sup>, as observed for instance during *Drosophila*  
29 germband elongation<sup>3</sup>. Nevertheless, the stress generated by the seam cells is  
30 anisotropic and globally oriented along the DV axis (see cyan box in Fig. 1a)<sup>2</sup>. The  
31 stress anisotropy results mainly from the presence of circumferential F-actin filament  
32 bundles in DV epidermal cells, which create a global stiffness anisotropy (see yellow  
33 box in Fig. 1a). The DV epidermal cells do not contribute to generate active stress  
34 (Fig. 1a), as their myosin II is kept mostly silent through the activity of the RhoGAP  
35 RGA-2<sup>1,2,4</sup>. The interplay between stress anisotropy in seam cells, stiffness anisotropy  
36 from the DV epidermis, and hydrostatic pressure resulting from the reduction of  
37 embryo diameter, induces a force oriented along the AP direction that is sufficient to  
38 extend the embryo until it reaches the 2-fold stage<sup>2</sup>.

39 Note that here as well as in the main text we refer to each elongation phase based  
40 on the ratio between the actual embryo length and that of the eggshell long axis,  
41 i.e. 1.7-fold or 2-fold means that the embryo has reached roughly 85 µm or 100 µm,  
42 respectively. Importantly, in mutant embryos which extend slower, we refer to  
43 embryo stages based on the length that a wild-type embryo would reach after the  
44 same time duration with  $t_0$  corresponding to the beginning of elongation (see  
45 extension curves in Fig. 2d and Movie 1).

46 For simplicity, let us call the net force in the AP direction produced by the epidermis  
47 the epidermal cell force ( $F_{epid}$ ). This force is not enough to explain the elongation up  
48 to the 4-fold stage, since genetic analysis has established that embryos with non-

49 functional muscles do not elongate beyond the 2-fold stage (Fig. 2b)<sup>5</sup>. Therefore,  
50 muscles provide a second active force driving elongation beyond the 2-fold stage,  
51 which we will call  $F_{muscles}$ .

52 During embryogenesis, muscles organize and assemble in four rows located under  
53 the epidermis (Fig. 1a). Muscles are attached to the extracellular matrix that  
54 separates them from the epidermis, and that in turn serves to anchor the epidermis  
55 through hemidesmosome-like junctions<sup>1</sup>. Muscle organization and maturation is a  
56 progressive process, such that muscle activity starts with small contractions at the 1.7-  
57 fold, which progressively become more robust. The mechanical activity of muscles  
58 can be summarized as an alternation of contractions followed by relaxation. Since  
59 muscles are tightly connected to the epidermis, their contractions locally and  
60 repeatedly induce an anterior-posterior compression and extension of the epidermis,  
61 which can be visualized through the displacement of the actin cables (Fig. 1b-c, Fig.  
62 S7). The stress exerted by muscle contractions on the epidermis induces a  
63 mechanotransduction pathway (2<sup>nd</sup> yellow box in Fig. 1a), which is essential to  
64 promote hemidesmosome maturation and embryo elongation<sup>8</sup>.

65

66 **1.2 Viscoplastic model.** The *C. elegans* epidermis can be modelled as a visco-elastic  
67 body, more specifically as a Kelvin-Voigt system with a spring and dashpot in  
68 parallel, subject to two main active forces: the epidermal force  $F_{epid}$ , which is a  
69 continuous positive force, and the muscle force  $F_{muscles}$ , which is a pulsatile force since  
70 muscles alternatively contract and relax. The first force is present since the beginning  
71 of elongation, whereas the second force starts only after the 1.7-fold stage. The  
72 elastic reaction of the epidermis to active forces can be captured by Hooke's law;  
73 the damped nature of the reaction can be expressed by a viscous term. Overall the

74 length of the embryo over time  $l(t)$  can be captured by the equation:

75  $\eta \frac{dl}{dt} = -k(l - \lambda) + F_{epid} + F_{muscles}$  (1)

76 where  $k$  is the body stiffness,  $\lambda$  is the worm resting length and  $\eta$  is the coefficient of  
77 viscosity. Inertia has been neglected given the low Reynolds number of the system.

78 Eq. (1) corresponds to the so-called Kelvin-Voigt viscoelastic model<sup>6,7</sup> that captures  
79 the behavior of viscoelastic solids under stress or deformation. For constant forces,  
80 the solution of Eq. (1) is given by:

81 
$$l(t) = \frac{F_{epid} + F_{muscles}}{k} (1 - e^{-t/\tau}) + \lambda \quad (2)$$

82 meaning that the length of the system relaxes to the plateau value  $\frac{F_{epid} + F_{muscles}}{k}$  in a  
83 relaxation time of  $\tau = \eta/k$ .

84  $F_{epid}$  can promote elongation until the 2-fold stage (Fig. S5a'). Beyond, the pulsatile  
85 force originating from muscles,  $F_{muscles}$ , alternates periods of positive, negative or null  
86 contribution, so that its temporal average  $\langle F_{muscles} \rangle_\theta$  is null:

87 
$$\langle F_{muscles} \rangle_\theta = \frac{1}{\theta} \int_0^\theta F_{muscles}(t) dt = 0, \text{ for } \theta = nT \quad (3)$$

88 where  $\theta$  is the integration period,  $T$  is the period and  $n$  is a positive integer. As a  
89 consequence, on average,  $F_{muscles}$  will not contribute to the steady state length ( $l_{ss}$ )  
90 of the embryo (see Fig. S5a-c) that is set by  $l_{ss} = \frac{F_{epid}}{k} + \lambda$ .

91 A way to introduce a positive contribution to embryo lengthening is to allow some  
92 plasticity, in the physical sense, or ability of the system to get reorganized. For  
93 example, let consider a stretching pulse due to muscle activity during which the  
94 embryo increases its length  $l(t)$  with an increment  $dl$ , such that the embryo will be

95 temporarily  $l(t)+dl$  long at the end of the pulse. During the subsequent relaxation  
 96 phase, due to elasticity in the system, the embryo should return to the initial length  $l(t)$   
 97 it had before muscles had locally extended it. However, if it undergoes a permanent  
 98 plastic deformation, then the body will permanently keep a portion of the stretched  
 99 length. This situation corresponds to a permanent rearrangement, and it has been  
 100 observed and modeled in biological systems undergoing stresses<sup>8,9</sup>. Similarly to<sup>9</sup>, a  
 101 simple mathematical solution to introduce plasticity consists in having an adjustable  
 102 resting length  $\lambda$  that increases linearly with the length  $l(t)$  according to:

$$103 \quad \frac{d\lambda}{dt} = \beta \frac{dl}{dt} H(\alpha_{DV}) \quad \text{if } \frac{dl}{dt} > 0 \text{ and } l - \lambda > \frac{F_c}{k} \quad (4)$$

104 where  $0 \leq \beta < 1$  is a proportionality factor called ‘plasticity factor’; the case of  $\beta = 0$   
 105 corresponds to an absence of plasticity. The condition  $\frac{dl}{dt} > 0$  ensures that there is  
 106 rearrangement only during the extension phases and the condition:  $l - \lambda > \frac{F_c}{k}$   
 107 means that the rearrangement takes place only if the applied force exceeds a  
 108 critical force  $F_c$ . The term  $H(\alpha_{DV})$  is the Heaviside step function, which expresses that  
 109 dorso-ventral rearrangement is possible only in presence of resistance. For the  
 110 description of  $\alpha_{DV}$  term, see next paragraph. Note that Eq. (4) is equivalent to  
 111  $\lambda = \lambda(0)(1 - \beta) + \beta l$  with  $\lambda(0)$  being both the length and the resting length at time  
 112 zero and  $F_c = 0$ . With these choices and with a constant positive force  $F$  Eq. (1) has  
 113 the following solution:

$$114 \quad l(t) = \frac{1}{(1-\beta)} \frac{F}{k} (1 - e^{-t(1-\beta)/\tau}) + \lambda(0) \quad (5)$$

115 Hence, the plasticity condition effectively reduces the body stiffness  $k$  to  $k(1 - \beta)$   
 116 enabling the system to reach a longer final size compared to the one allowed by the  
 117 Kelvin-Voigt system alone, and increasing the relaxation time. By introducing

118 plasticity like in Eq. (4), the body progressively gains length at each stretching phase  
119 (Fig S5d-d').

120

121 **1.3 The consequences of actin stability defects.** As reminded above, the intensity of  
122  $F_{epid}$  relies on two components: the constant contractility of the seam cell actomyosin  
123 network, and the stiffness of the actin cables in DV cells. We can then represent it  
124 like:

$$125 \quad F_{epid} = F_{seam} \alpha_{DV} \quad (6)$$

126 where the force  $F_{seam}$  represents the active force generated by myosin II in the  
127 lateral cells and  $\alpha_{DV}$  is the passive component given by the presence of actin  
128 filament bundles in the DV cells. The biomechanical significance of equation (6) is  
129 that both  $F_{seam}$  and  $\alpha_{DV}$  positively contribute to  $F_{epid}$ , and that if one is absent  $F_{epid}=0$ .  
130 This captures the fact that in the absence of myosin II there will be no pulling force  
131 because the active component is absent, and that if actin cables are lost myosin II is  
132 missing the resistance structure onto which it can pull, resulting in a null epidermis AP  
133 force.

134 As shown in the main text (Fig. 3), the absence of SPC-1 and PAK-1, combined with  
135 the mechanical input from muscles, induces actin integrity defects in DV cells. To  
136 translate this situation in mathematical terms, we chose to write the passive  
137 component  $\alpha_{DV}$  as follows:

$$138 \quad \frac{d\alpha_{DV}}{dt} = \gamma \frac{dl}{dt} \quad if \quad \frac{dl}{dt} < 0 \text{ and } \alpha_{DV} \geq 0 \quad (7)$$

139 where  $\gamma \geq 0$  is a proportionality factor defined as a 'tearing factor'. The condition

140     $\frac{dl(t)}{dt} < 0$  means that  $\alpha_{DV}$  decreases stepwise with time. In addition, we are imposing  
 141    that  $\gamma=0$  corresponds to an absence of tearing, like in wild-type embryos. The  
 142    biological significance of this choice is the following: in phases of length decrease  
 143    (net negative force), the overall circumference of the embryo should increase due  
 144    to volume conservation (Fig. S4). In a background of unstable actin filaments (like in  
 145    *spc-1 pak-1* double mutants) their resistance to stress originating from muscle activity  
 146    would not be maintained. For this reason,  $\alpha_{DV}$  should progressively decrease at each  
 147    cycle. The condition  $\alpha_{DV} \geq 0$  prevents  $\alpha_{DV}$  from assuming negative values. Thus with  
 148     $\alpha_{DV}$  decreasing,  $F_{epid}$  will progressively decrease, and as consequence the system  
 149    length will shorten (see Fig. S5e and Fig. 4e).

150

151    **1.4 Equations summary.** In summary, we describe the embryo body as a plastic  
 152    Kelvin-Voigt solid according to the following system of equations:

$$153 \quad \eta \frac{dl}{dt} = -k(l - \lambda) + F_{epid} + F_{muscles} \quad (1) \quad (\text{Kelvin-Voigt with adjusting resting length})$$

154    subject to  $F_{epid} + F_{muscles}$ )

$$155 \quad \frac{d\lambda}{dt} = \beta \frac{dl}{dt} H(\alpha_{DV}) \quad \text{if } \frac{dl}{dt} > 0, 0 \leq \beta < 1 \text{ and } l - \lambda > F_c/k \quad (5) \quad (\text{plasticity condition})$$

$$156 \quad \frac{d\alpha_{DV}}{dt} = \gamma \frac{dl}{dt} \quad \text{if } \frac{dl}{dt} < 0 \text{ and } \alpha_{DV} \geq 0 \quad (7) \quad (\text{tearing condition})$$

157    With  $F_{epid} = F_{seam}$   $\alpha_{DV}$  as described in Eq.(4).

158    We assume that  $\gamma=0$  for wild-type and *unc-112*, meaning that the resistance of dorso-  
 159    ventral actin filament bundles remains unaffected by the body length changes  
 160    caused by muscle activity.

161 The equations (1), (4), (5) and (7) have seven parameters:  $\eta$ ,  $k$ ,  $F_{seam}$ ,  $\alpha_{DV}(0)$ ,  $F_{muscles}$ ,  $\beta$   
162 and  $\gamma$ . In order to reduce the parameter space we fixed some of them:  
163 - for simplicity we set **k=1**;  
164 - from the laser ablation experiments performed in reference<sup>2</sup>, the relaxation  
165 time of epidermal actin filaments following the laser cut is in the order of a few  
166 seconds. Being the relaxation time in a Kelvin-Voigt system given by  $\tau = \eta/k$ ,  
167 we set  **$\eta=3$**  so that the relaxation time is 3 seconds.  
168 -  $F_{epid}$  is the multiplication of two parameters, and thus from the parameter  
169 point of view can be considered as a single parameter that we formally set to  
170  **$F_{seam}=1$**  letting  $\alpha_{DV}(0)$  as a free parameter.  
171 - The size of the critical force  $F_c$  has been chosen to be half  $F_{seam}$  ( **$F_c = 0.5$** ).  
172 Thereby, we consider that low intensity forces cannot trigger a plastic  
173 response.  
174 - Regarding  $F_{muscles}$ , we specified its details on the basis of the measured  
175 contraction durations for embryos between 1.7 and 2-fold stages (Fig. S7). For  
176 wild-type embryos, the duration of positive and negative periods has been set  
177 to 6 seconds and the period of null contribution has been set to 15 seconds,  
178 whereas for *spc-1* mutants and *spc-1 pak-1* double mutants the duration of  
179 non-null activity has been set to 3 seconds and the duration of null  
180 contribution is set to 15 seconds. In wild-type embryos, the intensity of  $F_{muscles}$   
181 has been left as a fit parameter together with  $\alpha_{DV}$ ,  $\beta$  and  $\gamma$  in order to be  
182 determined by comparing with the data. The muscle force amplitude for *spc-*  
183 *1* and *spc-1 pak-1* mutants has been set to **50% of the wt intensity** according  
184 to our experimental observations.  
185 To better adapt to the experimental observations, both  $F_{seam}$  and  $F_{muscles}$  have been  
186 modified by introducing an initial transient that sets their behavior from zero to the

187 regime of maximal intensity; the detailed form of these transients are reported in the  
188 paragraph ‘Refining model details’.

189

190 **1.5 Fitting procedure.** In order to determine the remaining four free parameters:  
191 intensity of  $F_{muscles}$ ,  $\alpha_{DV}(0)$  (the initial value of actin strength),  $\beta$  (the plasticity factor)  
192 and  $\gamma$  (tearing factor) we fitted different genotypes. We started with the muscle-  
193 defective *unc-112* and wild-type embryos. As shown in Figs. 2 and S3, their  
194 elongation rate is quite similar until the 2-fold stage, at which point *unc-112* embryos  
195 have no muscle force ( $F_{muscles}=0$ ), and they both have an identical actin pattern  
196 ( $\gamma=0$ ). Therefore, we fitted together the two elongation curves to find the values of  
197 the three parameters  $\alpha_{DV}(0)$ ,  $\beta$  and  $F_{muscles}$  that capture the main features of the two  
198 genotypes, and we refined the minor differences by allowing a 20% tolerance with  
199 respect to the parameters values determined through the common fit. To estimate  
200 the value of  $F_{muscles}$  intensity in *spc-1* and *spc-1 pak-1* embryos, we considered that it  
201 was half the wild-type value, based on the observation that the muscle  
202 contraction/relaxation cycles were roughly twice shorter in these embryos (Fig. S7).  
203 The notion that  $F_{muscles}$  is lower in *spc-1* mutant embryos is consistent with the  
204 observation that muscles make an angle of 20° with the anterior-posterior axis,  
205 instead of 6° in wild-type embryos, predicting that their input should be reduced<sup>10</sup>.  
206 The wild-type value of the plasticity factor was used as the upper limit for the  
207 variability range of  $\beta$  for *spc-1* and *spc-1 pak-1* embryos. We then proceeded by  
208 fitting the *spc-1* and *spc-1 pak-1* elongation curves to determine the values of  
209  $\alpha_{DV}(0)$ ,  $\beta$  and the tearing factor  $\gamma$  (see below for the method).

210 The best fit parameters were determined by minimalizing the following cost function:

$$\xi = \sum_g \sum_i [(curve_{data}(i) - curve_{model}(i))^2]_g \quad (8)$$

212 where  $curve_{data}(i)$  is the value of the data elongation curve at the time point  $i$  and  
213  $curve_{model}(i)$  is the solution of the model interpolated at the time point  $i$ ;  $g$  refers to  
214 the genotypes considered for a fit. To minimize the cost function, a Covariance Matrix  
215 Adaptation Evolution Strategy (CMA-ES) algorithm was used<sup>11</sup>. The algorithm has an  
216 available Matlab code at [http://www.lri.fr/~hansen/cmaes\\_inmatlab.html](http://www.lri.fr/~hansen/cmaes_inmatlab.html).

217 In the following table we report the values of the fitted parameters for the different  
218 genotypes presented in the Fig. 4j and S5f. Errors have been obtained by fitting the  
219 mean curves plus and minus their standard errors respectively and by taking the  
220 maximal deviation from the parameters obtained from the mean.

221

	wild-type	<i>unc-112</i>	<i>spc-1</i>	<i>spc-1 pak-1</i>
Initial actin stiffness $\alpha_{DV}(0)$	$1.06 \pm 0.05$	$1.13 \pm 0.01$	$0.84 \pm 0.03$	$0.76 \pm 0.03$
Plasticity factor $\beta$	$0.12 \pm 0.06$	$0.05 \pm 0.01$	$0.06 \pm 0.02$	$0.02 \pm 0.03$
Intensity $F_{muscles}$	$5.0 \pm 2.5$	$\emptyset$	2.5	2.5
Tearing factor $\gamma$	$\emptyset$	$\emptyset$	$0.04 \pm 0.01$	$0.12 \pm 0.01$

222

223 **1.6 Refining model details.** Ablation experiments in seam cells<sup>2</sup> have shown that the  
224 circumferential stress is not constant during development but increases from the 1.3-  
225 fold to 1.7-fold stages. To better adapt our model to this observation, we introduced  
226 a time dependent function for  $F_{epid}$  that saturates to a plateau value within a time  $\tau_s$ :

$$F_{epid}(t) = F_{seam} \alpha_{DV} (1 - \exp\left(-\frac{t}{\tau_s}\right))^{h_s} \quad (9)$$

228 where  $h_s$  is an exponent that sets the steepness of the function in reaching the  
229 plateau and  $F_{seam}$   $\alpha_{DV}$  is the plateau value. We set  $\tau_s=50$  min and  $h_s=4$ , since this  
230 choice produces slow elongation for the first 50 minutes, as was observed for all the  
231 genotypes (see Fig. 2). Much like the epidermis force, the muscle force  $F_{muscles}$  also  
232 starts at a small amplitude, then progressively evolves with a behavior similar to  
233 equation (8):

234

235

$$F_{muscles}(t) = \begin{cases} A \cdot \theta(t) \left(1 - \exp\left(-\frac{(t-t_{init})}{\tau_m}\right)\right)^{h_m} & \text{for } t > t_0 \\ 0 & \text{otherwise} \end{cases} \quad (10)$$

236

237 where  $A$  is the maximum amplitude,  $\theta(t)$  is the periodic function made of a  
238 composition of cosines described in Fig. S5c;  $h_m$  sets the steepness of the function to  
239 reach the plateau;  $t_0$  is the time at which muscles get active and  $\tau_m$  is the time  
240 necessary for the function to reach its plateau.

241 We started to measure the elongation curves immediately before the comma stage,  
242 which represents our initial time. We set  $t_{init}=90$  min, since around this point of  
243 elongation wild type embryos are 1.7-fold long and they start to contract muscles;  
244 we also assume that after the 2-fold stage the muscle force has reached its  
245 maximum amplitude, which is why we fixed  $\tau_m=15$  min (the time necessary for a wild  
246 type embryo to go from 1.7 to 2 fold;  $h_m$  has been arbitrarily set to 1).

247 The model summarized in Eqs. (5) and (9) has no plateau; however *C. elegans*  
248 embryos extend up to 4-fold within  $\leq 150$  minutes, then stay at this length for  $\sim 100$   
249 additional minutes before hatching. We do not know why the body length stops at 4-

250 fold and this issue is not the focus of this work. We can speculate that the ability of  
 251 the body to remodel is not illimited and may also be restricted by cuticle secretion. In  
 252 this framework, we can modify Eq.(5) by introducing a multiplicative term under the  
 253 form of a Hill function to account for the saturation of the elongation:

$$254 \quad \frac{d\lambda}{dt} = \beta \frac{dl}{dt} H(\alpha_{DV})Hill(\lambda) \quad \text{if } \frac{dl}{dt} > 0, \quad 0 \leq \beta < 1 \text{ and } l - \lambda > \frac{F_c}{k} \quad (11)$$

255 where  $Hill(\lambda) = \frac{L^d}{L^d + \lambda^d}$ , with  $L$  upper threshold for the resting length and  $d$  an  
 256 exponent<sup>12</sup>. We set **L=3.2** and **d=15** to account for a rapid saturation of elongation  
 257 after the 3.2-fold stage, since the wild type embryos show, after this length, a rapid  
 258 reduction of the elongation rate. By introducing these additional functions, we can  
 259 improve the agreement between the data and the model results (Fig. 4j). The  
 260 Equations presented above have been solved numerically by the Euler method  
 261 implemented in a Matlab script, with the choice of initial length  $l(0) = \lambda(0) = 1$ .

262 Below is a summary of the parameter values that we fixed on the basis of  
 263 experimental observations and therefore were not used as free parameters.

264

Spring	$k=1$
Dashpot	$\eta=3$
$F_{epid}$	$F_{seam}=1, \tau_s=50, h_s=4$
$F_{muscles}$	$\tau_m=15, h_m=1, t_{init}=90$
Saturation function	$L=3.2, d=15$
Critical force $F_c$	0.5

265  
 266

267 **1.7 Predictiveness of the model.** Here we test the model described above by  
268 comparing the predicted elongation curves with those observed with another  
269 genotype.

270 When muscle activity was compromised in *spc-1 pak-1* embryos, the retraction  
271 phenotype was prevented (Fig. 2). From equations (1) and (7), if  $F_{muscles}$  equals zero,  
272 then there should be no retraction. Moreover, by fitting the *unc-112; spc-1 pak-1*  
273 elongation curve we obtained a value of  $\alpha_{DV} = 0.64 \pm 0.04$ .

274

275 **1.8 Kelvin-Voigt-type model or Maxwell-type model?** In the present work we  
276 decided to model the *C. elegans* embryo as a visco-elastic solid with the ability to  
277 rearrange its resting length during elongation, and we show that this description can  
278 account both for elongation and retraction by changing the behavior of the  
279 epidermal force. The Maxwell model<sup>7</sup>, as a dashpot and a spring in series, would  
280 also account for elongation when the system is under the effect of a positive force.  
281 However, a Maxwell-type material keeps extending as soon as a positive force acts  
282 on it and this behavior would not account for the muscle-defective *unc-112*  
283 embryos. Indeed, these embryos elongate till about 2-fold under the effect of the  
284 epidermal force, but does not grow further in the absence of muscle activity,  
285 whereas a Maxwell model would predict that its elongation continues.

286

287 **2- Methods**

288 **Animal strains, conditions of maintenance**

289 The list of strains used is presented in Supplementary Table S4. Animals were  
290 propagated on NGM agar plates as described previously<sup>13</sup>. Animals were held at a  
291 standard 20°C temperature except for experiments implicating *sma-1(ru18); pak-*  
292 *1(tm403)*, in which case L4 animals were shifted to 15°C before egg laying and  
293 measures were performed on their offsprings.

294

295 **Yeast Two Hybrid Screening**

296 Yeast two-hybrid screening was performed by Hybrygenics Services (Paris, France).  
297 The bait component was the N-terminal 294 amino acids of PAK-1 (including the  
298 regulatory region of the protein) fused as a C-terminal fusion to LexA. The construct  
299 was used as a bait to screen at saturation a highly complex, random-primed  
300 *C.elegans* embryo cDNA library<sup>14</sup>. Screening involved a mating approach on a  
301 medium lacking Trp, Leu and His, supplemented with 0.5 mM 3-aminotriazole<sup>15</sup>. The  
302 strongest hits of the screen can be found in Supplementary Table 1. Reciprocal  
303 screens using the spectrin repeat #9 or the SH3 domains of SPC-1 as baits identified  
304 PAK-1 region 160-206, and no other meaningful prey in the context of the present  
305 study.

306

307 **RNAi enhancer screen and RNAi assays**

308 Two RNAi screens were performed in the *pak-1(tm403)* and in the *spc-1(ra409)*  
309 backgrounds along with a wild type control. A collection of 356 essential genes from  
310 the Ahringer RNAi library<sup>16</sup>, including adhesion proteins, signalling proteins,  
311 phosphatases, kinases, cytoskeleton-associated proteins and proteins important in

312 epithelial morphogenesis, was assembled (Table S1), based on a previous screen  
313 performed in the *git-1(tm1962)* background (C. Gally and M. Labouesse,  
314 unpublished). The screen was performed in liquid culture on 96-well plates and RNAi  
315 knockdown was induced by feeding as described<sup>17</sup>. The primary screen was based  
316 on enhanced lethality and body morphology defects; the secondary screen  
317 focused on very short larvae and elongation defects. We took DIC images for body  
318 length measurements and performed DIC timelapse imaging for the strongest  
319 candidates. For specific genes, RNAi was always induced by injection after  
320 preparing the double-stranded RNA (dsRNA) with the Ambion mMessage  
321 mMachine® kit and purifying the dsRNA with the Qiagen RNeasy® MinElute® Cleanup  
322 kit<sup>18</sup>. The embryos were analyzed from 24h to 48h post-injection.

323

#### 324 **Fluorescent translational reporter constructs**

325 A 12633 bp genomic sequence including the *spc-1* coding sequence and a 3 kb  
326 promoter was inserted in frame with the GFP coding sequence present in the  
327 pPD95.75 vector (Addgene, Cambridge USA). To create the *Ppak-1::pak-1::mKate*  
328 reporter construct, first an mKate-containing backbone was created by exchanging  
329 the GFP-coding sequence of the pML1572, *Plin-26::vab-10(ABD)::GFP* plasmid (Gally  
330 et al., 2009). In a following cloning step a 8204 bp genomic sequence, including the  
331 *pak-1* coding sequence and a 4.5 kb promoter was inserted in frame with the mKate  
332 coding sequence present in the vector.

333 To test if SPC-1::GFP could rescue the function of SPC-1, we first crossed the different  
334 transgenic animals of a wild type background with *mnDp33; spc-1(ra409)* animals  
335 (strain DM3409), and F1 transgenic males again with DM3409 to establish *mnDp33;*  
336 *spc-1(ra409); Ex[spc-1::GFP]*. Rescuing transgenes were recognized because all

337 viable progeny was GFP-positive and all (or most) non-viable progeny was GFP-  
338 negative, reflecting the loss of the *mnDp33* balancer. To attempt *mnDp33*  
339 segregation, we repeatedly transferred single GFP-positive mothers over four  
340 generations and examined their progeny, starting from at least two independent  
341 extrachromosomal arrays per construct. Thereby, we successfully obtained viable  
342 *spc-1(ra409); Ex[Pspc-1::spc-1(+)::gfp]* animals, and then viable *spc-1(ra409) pak-*  
343 *1(tm403); Ex[Pspc-1::spc-1(+)::gfp]* animals through crossing and meiotic  
344 recombination, which segregated very short retracted GFP-negative embryos. For  
345 the FHOD-1 constitutively active construct, a 8283 bp genomic sequence of *fhod-1*  
346 (gift from David Pruyne<sup>19</sup>) deleted for part of the FH2 domain and the DAD domain  
347 was inserted under the control of the epidermis-specific 432 bp *dpy-7* promoter.  
348 Deletion of the DAD alone was obtained by inserting back the FH2 domain in the  
349 FH2/DAD deleted construct using Hifi DNA assembly cloning kit (New England  
350 Biolabs); the FH1/FH2 deleted construct was obtained by deleting the FH1 domain  
351 using the Q5 site directed mutagenesis kit protocol (New England Biolabs). All cloning  
352 steps relied on the use of the Phusion High-Fidelity DNA Polymerase reaction kit (Fisher  
353 Thermo-Scientific); the constructs were subsequently verified by sequencing. The  
354 constructs were injected at 10 ng/μl plasmid construct, with 150 ng/μl pBSK + 5 ng/μl  
355 pCFJ90 (*P<sub>myo-2</sub>::mcherry*) as co-injection markers for the *spc-1::gfp* constructs, or 100  
356 ng/μl pRF4 (*rol*) co-injection marker for *pak-1::mKate*.

357

### 358 **Fluorescence imaging**

359 DIC images for time-lapse videos were obtained using a Leica DM6000 microscope  
360 with a Leica LAS-AF software, using a Leica DMRXA2 upright microscope equipped  
361 with a Peltier platform. Observations were done under a 40X oil immersion objective.

362 Mothers were cut up to gain early-staged embryos, which were then transferred  
363 onto thin 5% soft agarose pads in a drop of M9. Z stack image series with a 1,5 µm Z  
364 step distance were taken in every 5 minutes during 6 hours. ImageJ software was  
365 used to quantify the embryonic length from the end of ventral enclosure/onset of  
366 elongation, by taking a “segmented line” through the midline of the embryos from  
367 head to tail. To image the coupling between actin bundles displacement in the  
368 epidermis and muscle contractions, we used a double reporter strain carrying the  
369 epidermal *Pdpy-7::LifeAct::GFP* and muscle *Pmyo-3::his-24::mCherry* transgenes  
370 (ML2113, see Table S4), and a spinning-disk DMI6000 Leica microscope equipped  
371 with an Andor software (experiments for Fig. 1). Series of five Z planes (1 epidermal +  
372 4 muscle) were imaged continuously for 5 min, with 0,5 µm Z steps and no averaging.  
373 The time interval between two Z series was 360 ms. The measurement of actin  
374 displacement was done according to the same strategy, and was done using a  
375 CSUX1-A1 spinning-disk mounted on a Zeiss Axio Observer Z1 inverted microscope  
376 with a Roper Evolve camera controlled by the Metamorph software, and a 100x oil  
377 immersion objective (experiments for Fig. S9). A Z-stack of 4 focal planes with 0,5 µm  
378 step size was acquired using a streaming acquisition mode. The time between two  
379 acquisitions was 0.41 second during 300 time frames. To synchronize embryos,  
380 mothers were put on an empty NGM agar plate to lay eggs for a short time window,  
381 and embryos were left to develop until the stage of interest. (For the analyse of the  
382 contraction see next section on **Image analysis**. To analyse the *in vivo* co-localisation  
383 between PAK-1::mKate, ABD::mcherry and SPC-1::GFP, we used the Zeiss/Roper  
384 spinning disk microscope under a 100X oil immersion objective, keeping the laser  
385 intensity at a constant level throughout the experiments. Image processing and  
386 computing the co-localisation coefficient was done using the Volocity software.

387

388 **Image analysis and quantification of actin filament contraction, continuity and**  
389 **orientation**

390 The analysis of mechanical displacement in the epidermis was performed on the  
391 movies of the dorso-ventral actin layer by measuring the distance over time  
392 between two landmarks across the region of contraction. The landmarks were set  
393 manually on a frame showing relaxed tissue and tracked all over the contraction till  
394 the subsequent relaxed state. Landmarks tracking was performed using a statistical  
395 template matching approach<sup>20</sup>. The method was implemented as an ImageJ plugin  
396 (<http://sites.imagej.net/Julienpontabry/>), giving as output the landmarks locations,  
397 their distance across time and the Kymographs. The curves show a pre-contraction  
398 state, a minimum (the maximal contraction point) and an ending part where the  
399 distance progressively increases again (see Fig. 1B'' and Fig. S7). After a smoothing  
400 and interpolation of the curves, the starting, ending and maximal contraction points  
401 were extracted by studying the time derivative of the distance and by setting a  
402 threshold on the distance itself. Finally the contraction time was computed as the  
403 difference between the ending time and the initial time. The analysis of the curves  
404 and statistics were done using a MatLab script. All images were analysed using the  
405 ImageJ (Fiji) software (NIH, Bethesda, Maryland, USA; <http://rsb.info.nih.gov/ij/>) and  
406 MATLAB R2014b (The MathWorks Inc., Natick, MA). To study the features of actin  
407 pattern, we imaged embryos that were put to sleep by oxygen deprivation through  
408 a high concentration of bacteria with the Zeiss/Roper spinning-disk using a 100X oil  
409 immersion objective. For each experiments, a Z-stack of 16 focal planes with 0,2 µm  
410 step size was acquired. On the original maximum z projection created by imageJ, a  
411 manual ROI was defined on the dorso-ventral cells (Fig. 3) from which a high pass  
412 filter in the Fourier space was applied to select only structures smaller than 10 pixel of  
413 diameter (Fig. 3).

414

415 **Continuity:** The filtered ROIs were binarized by setting to one all the pixels with a  
416 value bigger than zero and setting to zero all the other pixels. The resulting structures  
417 were then fitted by ellipses from which the length of the Major axis was extracted as  
418 a measure of the length of the actin filament. The longer actin filaments are those  
419 presenting a more uniform fluorescence along their length (showing higher  
420 continuity). By contrast, short segments result from discontinuity in the fluorescence  
421 signal. To avoid noise only segments longer than 4 pixels have been considered for  
422 the analysis.

423

424 **Anisotropy of the orientation:** The same filtered ROI used for continuity measurements  
425 were used to measure the distribution of cable orientation. Fast Fourier Transform  
426 (FFT) of these ROIs was computed in order to work in the frequency domain and  
427 more easily identify repetitive patterns. The resulting power spectrum of the ROIs was  
428 represented in polar coordinates in order to extract the distribution of angles of ROI  
429 pattern<sup>21</sup>. The method was implemented in an ImageJ plugin  
430 (<http://sites.imagej.net/Julienpontabry/>), giving as output the angular distribution. In  
431 order to compare the distributions coming from different images the distributions  
432 were normalized by their integral (Fig. 3). The more the pattern consists in structures  
433 oriented in a preferred direction (the more anisotropic), the highest is the peak of the  
434 distribution in that direction. In the case of an isotropic pattern, the angular  
435 distribution should show a flat behavior. As an estimate of the pattern anisotropy, the  
436 prominence of the highest peak of the angular distribution was considered (Fig. 3  
437 and Fig. S4). The analysis of the angular distributions and statistics was performed by  
438 a MatLab script. All images were analysed using the ImageJ (Fiji) software (NIH,  
439 Bethesda, Maryland, USA; <http://rsb.info.nih.gov/ij/>) and MATLAB R2014b (The

440 MathWorks Inc., Natick, MA). All matlab scripts used for the present analysis are  
441 available upon request.

442

443 **Statistical Analysis**

444 For elongation curves, standard deviation was measured. For L1 length  
445 measurement and rescue experiments we perform unpaired t-test and ANOVA test  
446 using GraphPad Prism 5.00 (San Diego, California, USA) and Excel. For contraction  
447 time, actin continuity and orientation, we applied for all genotypes a paired t-test  
448 using Matlab.

449

450

451 **3-Supplementary figures**

452 **Supplementary Figure 1:** Local bending of epidermal actin filaments due to muscle  
453 contractions

454 **(a-c)** Displacement of actin filament marked by LifeAct::GFP at three time points in  
455 wild-type embryos. Note their local bending (yellow box). Scale bar, 10  $\mu$ m.

456

457 **Supplementary Figure 2:** Genes required to maintain embryonic elongation.

458 **(a-g)** The proteins GIT-1 and PIX-1 are acting upstream of PAK-1 in the mechano-  
459 transduction pathway promoted by muscle contractions, and their loss in the  
460 absence of *spc-1* also triggers a retraction phenotype. **(a)** Elongation curves and **(b-**  
461 **g)** terminal phenotypes of **(b)** *pak-1(tm403)*; **(c)** *git-1(tm1962)*; **(d)** *pix-1(gk416)*; **(e)**  
462 *spc-1(RNAi)* *pak-1(tm403)*; **(f)** *git-1(tm1962)* *spc-1(RNAi)* **(g)** *spc-1(RNAi)* *pix-1(tm416)*.

463 **(h-k)** The *pak-1(tm403)* mutation also showed synergistic body morphology defects  
464 when combined with the null allele *sma-1(ru18)* in the apical  $\beta$ -spectrin SMA-1, but  
465 not as pronounced as for loss of the  $\alpha$ -spectrin SPC-1. Quantification of the length at  
466 hatching **(h)** and terminal phenotypes of **(i)** *pak-1(tm403)*, **(j)** *sma(ru18)*, **(k)**  
467 *sma(ru18)*; *pak-1(tm403)* L1 hatchlings. **(l)** Elongation curves and **(m-n)** terminal  
468 phenotypes of **(m)** *unc-112(RNAi)* (n=5) and *unc-112(RNAi)*; *pak-1(tm403)* (n=8)  
469 embryos. **(o)** Terminal phenotype of *unc-112(RNAi)*; *spc-1(ra409)* obtained by  
470 inducing *unc-112(RNAi)* in the strain ML2436 bearing a rescuing extrachromosomal  
471 *spc-1::gfp* array and looking for embryos having lost the array; due to high stability of  
472 the array few embryos were obtained despite numerous repeats (n=4), which all had  
473 the phenotype illustrated here and is similar to that of *spc-1(ra409)* alone. Scale bars:  
474 17  $\mu$ m **(b-g; m-o)**; 50  $\mu$ m **(i- k)**.

475

476 **Supplementary Figure 3: PAK-1 and SPC-1 colocalized with actin filaments**

477 **(a)** Distribution of PAK-1::mKate in a late embryo (n=20). Enlarged pictures of PAK-1  
478 showing a filamentous distribution in the dorso-ventral epidermis similar to actin  
479 filaments. Scale bar: 25  $\mu$ m. **(b)** Fluorescence pictures of PAK-1::mKate (red) and SPC-  
480 1::GFP (green): the panel shows the colocalization image for the most apical focal  
481 planes (top image), and full XZ (green panel) and YZ (red panel) projections. The  
482 level of co-localization is high based on Pearson's correlation coefficient (0.7-0.9,  
483 n=20). The highest level of co-localization is detected at the apical cortex. **(c)**  
484 Fluorescence pictures of *Plin-26*::VAB-10(ABD)::mCherry (red) and SPC-1::GFP (green):  
485 the panel shows the colocalization image for the most apical focal planes (top  
486 image), and full XZ (green panel) and YZ (red panel) projections. The level of co-  
487 localization is high based on Pearson's correlation coefficient (0.7-0.9, n=8). The co-  
488 localization is almost exclusively detected at the apical cortex. The gene *lin-26* drives  
489 expression in the epidermis; VAB-10(ABD) corresponds to the two actin-binding  
490 domains (calponin homology) of the protein VAB-10. Scale bar, 10  $\mu$ m.

491

492 **Supplementary Figure 4:** Actin filament continuity and orientation at three elongation  
493 stages

494 Actin filaments were visualised using a *Pepid*::*Lifeact*::GFP construct and  
495 characterised as outlined in Fig. 3a (the *Pepid* promoter corresponds to *Pdpy-7*). **(a)**  
496 Actin filament continuity. The graph represents the length (in pixels) along the  
497 circumferential axis of actin filaments in early, mid and late (corresponding to 1.7-  
498 fold, 2-fold and 3-fold equivalent stages in a wild-type embryo, respectively)  
499 embryos of wild-type (early n=12, mid n=19, late n=16), *pak-1(tm403)* (early n=16, mid  
500 n=21, late n=16), *spc-1(RNAi)* (early n=15, mid n=21, late n=20), and *spc-1(RNAi)* *pak-*  
501 *1(tm403)* (early n=12, mid n=17, late n=26) genotypes. **(b)** Actin filament orientation

502 based on Fast Fourier Transform and binarisation. Wild type (early n=12, mid n=18,  
503 late n=14), *pak-1(tm403)* (early n=16, mid n=20, late n=16), *spc-1(RNAi)*(early n=14,  
504 mid n=18, late n=18), and *pak-1(tm403) + spc-1(RNAi)* (early n=12, mid n=18, late  
505 n=21). Note that the characteristics of actin filaments in *spc-1(RNAi)* *pak-1(tm403)*  
506 embryos differ mostly at the equivalent of the two-fold stage when muscles become  
507 active. At earlier and later stages, *spc-1(RNAi)* embryos and *spc-1(RNAi)* *pak-*  
508 *1(tm403)* embryos become similar. **(c-f)** Epidermal actin filaments visualized with the  
509 Pepid::Lifeact::GFP construct in wild-type (C), *spc-1(RNAi)* *pak-1(tm403)* (D) embryos  
510 (panels are from Fig. 3). \* $<0.05$ ; \*\* $<0.001$ ; \*\*\* $<0.0001$ ; ns, not significant.

511

512 **Supplementary Figure 5:** Change in embryo diameter during elongation

513 **(a-b'')** Fluorescence micrographs of embryos expressing the *Pepid::Lifeact::GFP*  
514 construct in the epidermis at three elongation stages early, middle and late  
515 (corresponding to 1.7-fold, 2-fold and 3-fold equivalent stages in a wild-type embryo,  
516 respectively) for wild-type **(a-a'')** and *spc-1(RNAi)* *pak-1(tm403)* embryos **(b-b'')**; the  
517 *Pepid* promoter corresponds to *Pdpy-7*. The yellow lines correspond to the segments  
518 used to measure the dorso-ventral width of the V1 seam cell. **(c)** Quantification of  
519 the average V1 cell width normalized to the initial width during elongation in four  
520 genotypes. **(d)** Quantification of the average dorso-ventral width at the level of the  
521 V1 seam cell, which was calculated using the measured embryo length and V1 cell  
522 width, taking into consideration the conservation of the total embryo volume. Each  
523 point in panel **(c)** and **(d)** represents between 7 and 21 embryos; error bars are  
524 standard errors. A notable feature of *spc-1(RNAi)* *pak-1(tm403)* embryos is that the  
525 circumferential dimension of the seam cells decreased much more than that of their  
526 DV cell, which most likely reflects the actin filament integrity defects combined with  
527 a  $F_{\text{seam}}$  force largely unchanged.

528

529 **Supplementary Figure 6:** Time-dependent length of a Kelvin-Voigt model in different  
530 conditions.

531 **(a-a')** A generic Kelvin-Voigt system subject to a constant force  $F_{epid}$  and its  
532 predicted elongation change using  $F_{epid}=0.85$  (A'). **(b-b')** A similar system subject to  
533 two forces,  $F_{epid}$  and an oscillating force  $F_{muscles}$  with the properties depicted in (E),  
534 and predicted elongation change using  $F_{epid}=0.85$  (B'). As the pulsatile force induces  
535 both compression and stretching (see Fig. S6), its net input on elongation is transient  
536 and the system oscillates around the maximal value reached without  $F_{muscles}$ . **(d-d')** A  
537 Kelvin-Voigt system with mechanical plasticity introduced according to Eqs. (1,4-7),  
538 and predicted elongation change using  $F_{epid}=0.85$ ,  $\beta=0.10$  and  $F_c=0$  according to  
539 Eqs. (1,4-7). **(e)** A Kelvin-Voigt system in which the plasticity is defective ( $\beta=0$ ), and  
540 there is actin tearing according to Eq. (7) inducing a progressive reduction of  $F_{epid}$ ,  
541 and predicted elongation change using  $F_{epid}=0.85$ , with an initial value of the passive  
542 component  $\alpha_{DV}(t=0)=1$  and the tearing factor  $\gamma=0.15$  (D'). **(e' Inset)** Behavior of  
543  $\alpha_{DV}(t)$ . **(c)** In all conditions  $F_{muscles}$  is a periodic function with positive and negative  
544 steps of duration of 6 seconds alternating with periods of null value of duration 15  
545 seconds modulated by a cosine function. In **(a-e')** the elastic constant of the spring is  
546  $k=1$ , the initial resting length has the value  $\lambda(t=0)=1$ , and the viscosity value is  $\eta=10$ . **(f)**  
547 Result of the fit for the following genotypes: *wt*, *spc-1* *pak-1*, *unc-112* and *spc-1*  
548 according to Eqs. (1,4-7). The values of the parameters are specified in paragraphs  
549 1.4, 1.5 and 1.6.

550

551 **Supplementary Figure 7:** Comparable retraction phenotypes after the combined loss  
552 of SPC-1 and PAK-1 or SPC-1 and FHOD-1

553 (a) Elongation curves of the single and double deficient embryos indicated on the  
554 left, (b-h) and corresponding terminal phenotypes at hatching: wild-type (n=5),  
555 *fhod-1(tm2363)* (n=6) *fhod-1(RNAi)* (n=7) *pak-1(tm403)* (n=5) *fhod-1(RNAi)*;  
556 *pak-1(tm403)* (n=7), *spc-1(RNAi)* *pak-1(tm403)* (n=8), *fhod-1(tm2363);spc-1(RNAi)*  
557 (n=9). Scale bar, 25  $\mu$ m.

558

559 **Supplementary Figure 8:** PAK-1 and FHOD-1 form aggregates in *spc-1(RNAi)* loss of  
560 function.

561 (a-a') PAK-1::GFP localisation in wild-type and *spc-1(RNAi)* embryos. Yellow box, area  
562 enlarged below the panel. Note the punctae in SPC-1 deficient embryos. (b-b')  
563 FHOD-1 localization in wild-type and *spc-1(RNAi)* embryos. Note the aggregates  
564 (arrowheads). Note also that FHOD-1::GFP displayed a filamentous organization  
565 reminiscent of actin filaments. Scale bar: 10  $\mu$ m.

566

567 **Supplementary Figure 9:** Actin displacement ratio

568 (a-d) Individual displacement tracks of actin filaments visualized with a *Pdpy-*  
569 7::*Lifeact::GFP* marker specifically expressed in the epidermis of wild type (a), *pak-*  
570 1(*tm403*) (b), *spc-1(RNAi)* (c) and *spc-1(RNAi)* *pak-1(tm403)* (d) embryos at a stage  
571 equivalent to 2-fold in a wild-type embryo. Scale bar: 10  $\mu$ m. (e) Typical kymographs  
572 of *Pepid::Lifeact::GFP*-labeled actin filaments in wild-type and *spc-1(RNAi)* *pak-*  
573 1(*tm403*) embryos from which the tracks in a-d were derived. Yellow dots correspond  
574 to landmarks for quantitative analysis. (f) Quantification of the displacement duration  
575 in (N=embryo/ n=contraction): wild-type, N=11/n=51; *pak-1(tm403)*, N=11/n=26; *spc-*  
576 1(*RNAi*), N=11/n=73; *spc-1(RNAi)* *pak-1(tm403)*, N=11/n=89. \*<0,05; \*\*<0,001;  
577 \*\*\*<0,0001; ns, not significant.

578

579 **4-Caption for movies**

580 **Movie 1:** Combined DIC timelapse movie. Image acquisition was every 5 minutes in  
581 wild-type, *pak-1(tm403)*, *spc-1(RNAi)*, *spc-1(RNAi)* *pak-1(tm403)* embryos. Scale Bar,  
582 10 µm.

583 **Movie 2:** Combined DIC timelapse movie of *unc-112(RNAi)* and *unc 112(RNAi)*; *spc-*  
584 *1(RNAi)* *pak-1(tm403)* embryos. Scale Bar, 10 µm.

585 **Movie 3:** Combined DIC timelapse movies of *spc-1(ra409)* and *fmod-1(RNAi)*; *spc-*  
586 *1(ra409)* embryos. Scale Bar, 10 µm.

587 **Movie 4:** Fluorescence movie showing the displacement of actin filaments labelled  
588 with *Pdpy-7::lifeact::GFP* in the epidermis. Time acquisition is 0.41 s in wild-type, *pak-*  
589 *1(tm403)*, *spc-1(RNAi)* and *spc-1(RNAi)* *pak-1(tm403)* embryos. Scale Bar, 10 µm.

590

591

592

593 **5-Supplementary references**

594 1 Vuong-Breder, T. T., Yang, X. & Labouesse, M. C. *C. elegans* Embryonic  
595 Morphogenesis. *Curr Top Dev Biol* **116**, 597-616,  
596 doi:10.1016/bs.ctdb.2015.11.012 (2016).

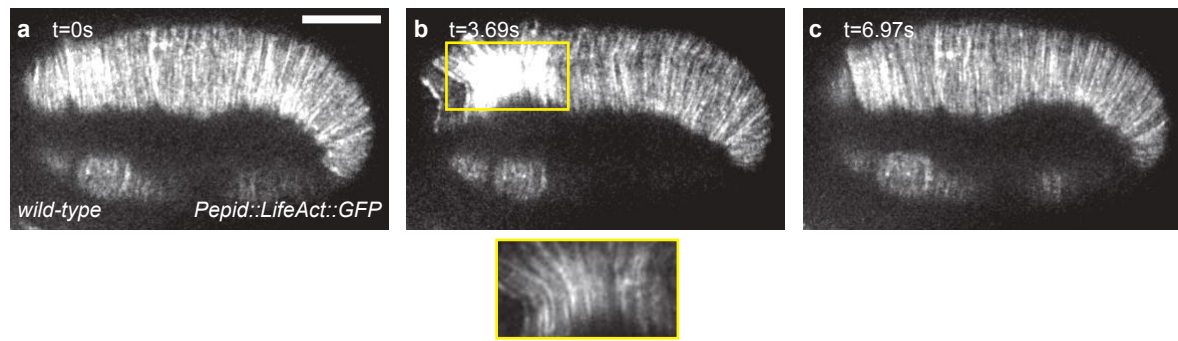
597 2 Vuong-Breder, T. T., Ben Amar, M., Pontabry, J. & Labouesse, M. The interplay of  
598 stiffness and force anisotropies drive embryo elongation. *eLife* **6**,  
599 doi:10.7554/eLife.23866 (2017).

600 3 Rauzi, M., Lenne, P. F. & Lecuit, T. Planar polarized actomyosin contractile flows  
601 control epithelial junction remodelling. *Nature* **468**, 1110-1114, doi:nature09566  
602 [pii]

603 10.1038/nature09566 (2010).

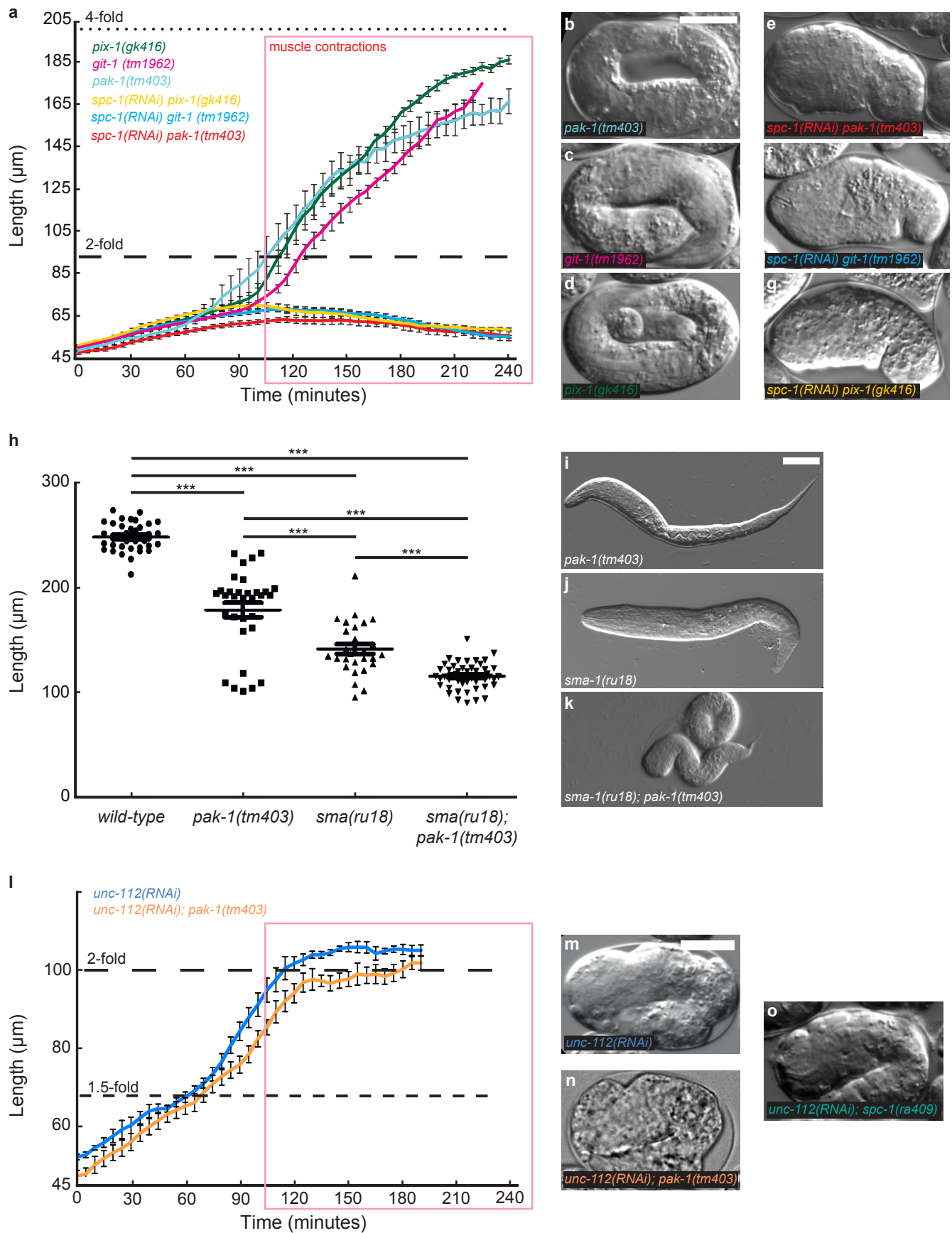
604 4 Diogon, M. *et al.* The RhoGAP RGA-2 and LET-502/ROCK achieve a balance of  
605 actomyosin-dependent forces in *C. elegans* epidermis to control morphogenesis.  
606 *Development* **134**, 2469-2479, doi:dev.005074 [pii]

- 607 10.1242/dev.005074 (2007).
- 608 5 Williams, B. D. & Waterston, R. H. Genes critical for muscle development and  
609 function in *Caenorhabditis elegans* identified through lethal mutations. *J Cell Biol*  
610 **124**, 475-490. (1994).
- 611 6 Vincent, J. in *Structural Biomaterials: Third Edition* 1-28 (Princeton University  
612 Press, 2012).
- 613 7 Meyers, M. A. & Chawla, K. K. *Mechanical Behavior of Materials*. (Cambridge  
614 University Press, 2008).
- 615 8 Dubrovinski, K., Swan, M., Polyakov, O. & Wieschaus, E. F. Measurement of  
616 cortical elasticity in *Drosophila melanogaster* embryos using ferrofluids. *Proc  
617 Natl Acad Sci U S A* **114**, 1051-1056, doi:10.1073/pnas.1616659114 (2017).
- 618 9 Munoz, J. J. & Albo, S. Physiology-based model of cell viscoelasticity. *Phys Rev E  
619 Stat Nonlin Soft Matter Phys* **88**, 012708, doi:10.1103/PhysRevE.88.012708  
620 (2013).
- 621 10 Norman, K. R. & Moerman, D. G. Alpha spectrin is essential for morphogenesis  
622 and body wall muscle formation in *Caenorhabditis elegans*. *The Journal of cell  
623 biology* **157**, 665-677, doi:10.1083/jcb.200111051 (2002).
- 624 11 Hansen, N. & Ostermeier, A. Completely derandomized self-adaptation in  
625 evolution strategies. *Evol Comput* **9**, 159-195,  
626 doi:10.1162/106365601750190398 (2001).
- 627 12 Alon, U. (Chapman & Hall/CRC, Boca Raton, 2007).
- 628 13 Brenner, S. The genetics of *Caenorhabditis elegans*. *Genetics* **77**, 71-94 (1974).
- 629 14 Gomes, J. E. et al. Microtubule severing by the katanin complex is activated by  
630 PPFR-1-dependent MEI-1 dephosphorylation. *J Cell Biol* **202**, 431-439,  
631 doi:10.1083/jcb.201304174 (2013).
- 632 15 Fromont-Racine, M., Rain, J. C. & Legrain, P. Toward a functional analysis of the  
633 yeast genome through exhaustive two-hybrid screens. *Nat Genet* **16**, 277-282,  
634 doi:10.1038/ng0797-277 (1997).
- 635 16 Kamath, R. S. et al. Systematic functional analysis of the *Caenorhabditis elegans*  
636 genome using RNAi. *Nature* **421**, 231-237 (2003).
- 637 17 Gally, C., Zhang, H. & Labouesse, M. Functional and Genetic Analysis of VAB-10  
638 Spectraplakin in *Caenorhabditis elegans*. *Methods in Enzymology* **in press**,  
639 doi:<http://dx.doi.org/10.1016/bs.mie.2015.05.005> (2015).
- 640 18 Bosher, J. M. et al. The *Caenorhabditis elegans* *vab-10* spectraplakin isoforms  
641 protect the epidermis against internal and external forces. *J Cell Biol* **161**, 757-  
642 768 (2003).
- 643 19 Mi-Mi, L., Votra, S., Kemphues, K., Bretscher, A. & Pruyne, D. Z-line formins  
644 promote contractile lattice growth and maintenance in striated muscles of *C.  
645 elegans*. *J Cell Biol* **198**, 87-102, doi:10.1083/jcb.201202053 (2012).
- 646 20 Matthews, I., Ishikawa, T. & Baker, S. The template update problem. *IEEE Trans  
647 Pattern Anal Mach Intell* **26**, 810-815, doi:10.1109/TPAMI.2004.16 (2004).
- 648 21 Gonzalez, R. C. & Woods, R. E. *Digital Image Processing (3rd Edition)*. (Prentice-  
649 Hall, Inc, 2006).
- 650
- 651



**Supplementary Figure 1:** Local bending of epidermal actin filaments due to muscle contractions

(a-c) Displacement of actin filament marked by LifeAct::GFP at three time points in wild-type embryos.  
Note their local bending (yellow box). Scale bar, 10  $\mu\text{m}$ .



**Supplementary Figure 2:** Genes required to maintain embryonic elongation.

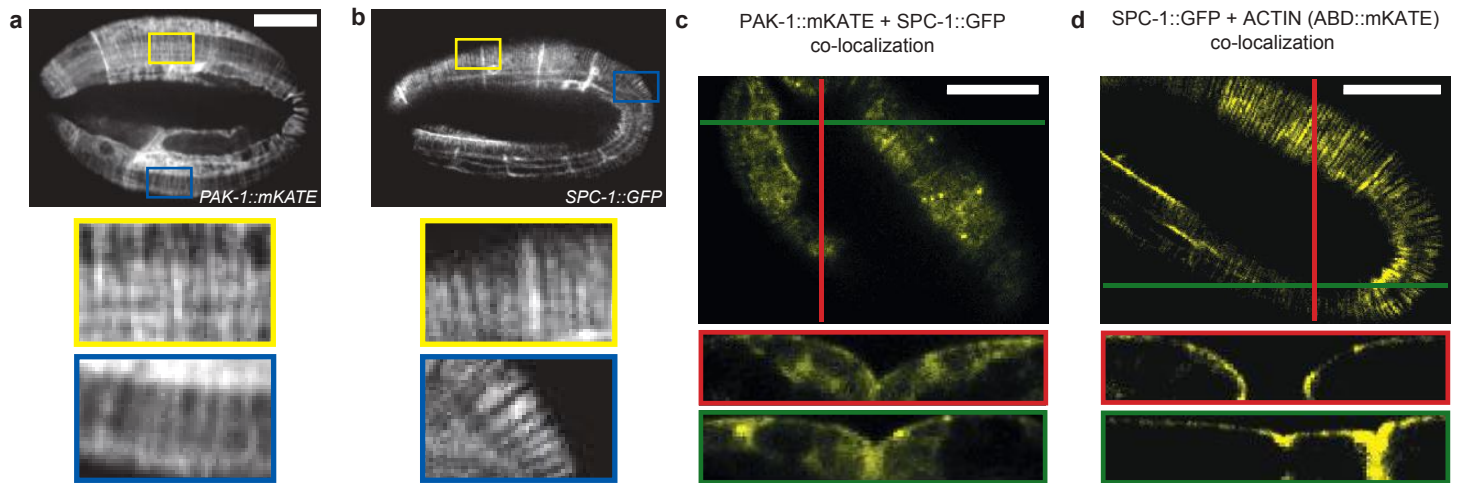
(a-g) The proteins GIT-1 and PIX-1 are acting upstream of PAK-1 in the mechano-transduction pathway promoted by muscle contractions, and their loss in the absence of spc-1 also triggers a retraction phenotype.

(a) Elongation curves and (b-g) terminal phenotypes of (b) *pak-1(tm403)*; (c) *git-1(tm1962)*; (d) *pix-1(gk416)*; (e) *spc-1(RNAi)* *pak-1(tm403)*; (f) *git-1(tm1962)* *spc-1(RNAi)* (g) *spc-1(RNAi)* *pix-1(tm416)*.

(h-k) The *pak-1(tm403)* mutation also showed synergistic body morphology defects when combined with the null allele *sma-1(ru18)* in the apical  $\beta$ -spectrin SMA-1, but not as pronounced as for loss of the  $\alpha$ -spectrin SPC-1. Quantification of the length at hatching (h) and terminal phenotypes of (i) *pak-1(tm403)*, (j) *sma(ru18)*, (k) *sma(ru18); pak-1(tm403)* L1 hatchlings.

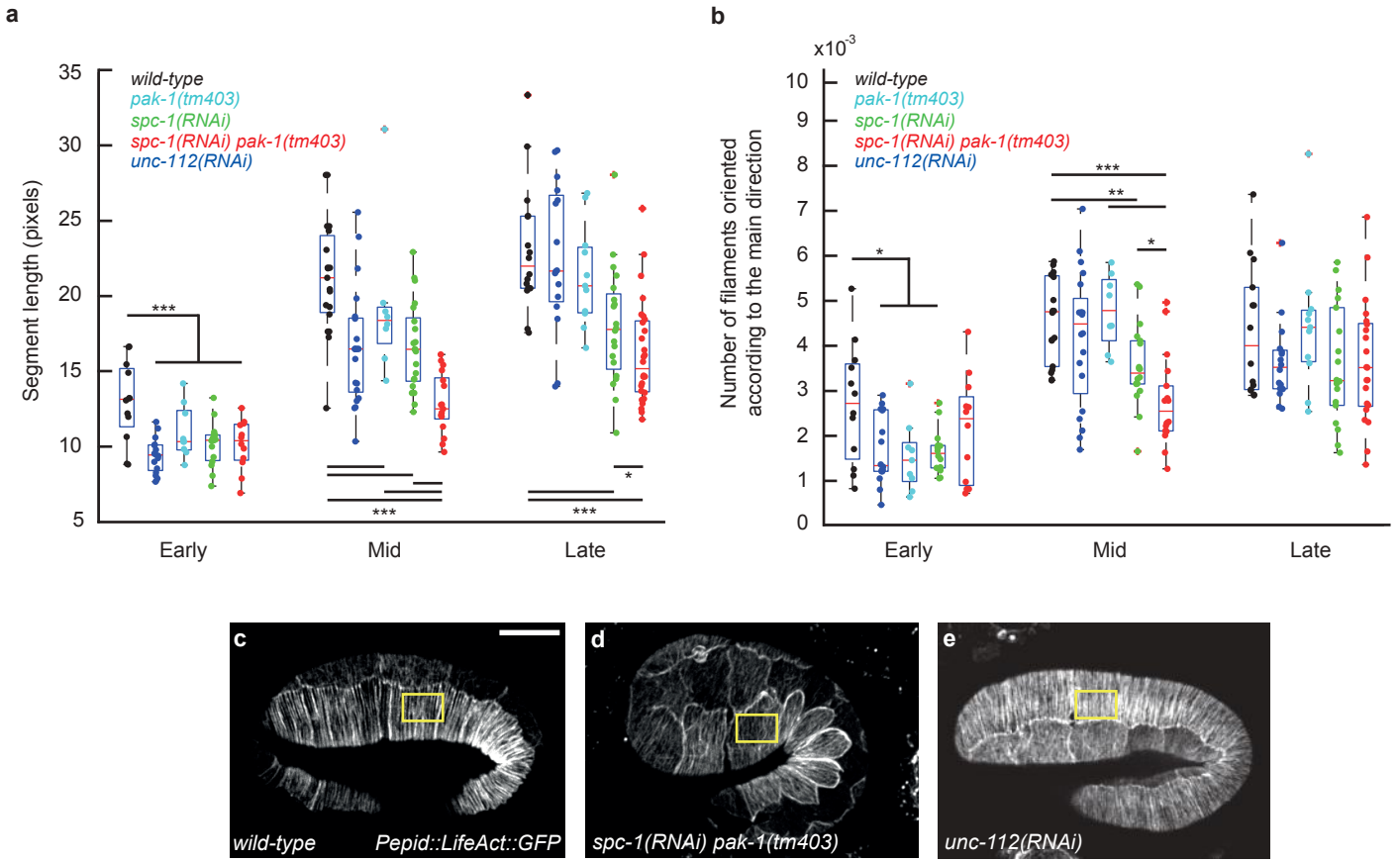
(l) Elongation curves and (m-n) terminal phenotypes of (m) *unc-112(RNAi)* (n=5) and *unc-112(RNAi); pak-1(tm403)* (n=8) embryos.

(o) Terminal phenotype of *unc-112(RNAi); spc-1(ra409)* obtained by inducing *unc-112(RNAi)* in the strain ML2436 bearing a rescuing extrachromosomal *spc-1::gfp* array and looking for embryos having lost the array; due to high stability of the array few embryos were obtained despite numerous repeats (n=4), which all had the phenotype illustrated here and is similar to that of *spc-1(ra409)* alone. Scale bars: 17  $\mu\text{m}$  (b-g; m-o); 50  $\mu\text{m}$  (i-k).



**Supplementary Figure 3:** PAK-1 and SPC-1 colocalized with actin filaments

- (a) Distribution of PAK-1::mKate in a late embryo (n=20). Enlarged pictures of PAK-1 showing a filamentous distribution in the dorso-ventral epidermis similar to actin filaments. Scale bar: 25 μm.
- (b) Fluorescence pictures of PAK-1::mKate (red) and SPC-1::GFP (green):  
the panel shows the colocalization image for the most apical focal planes (top image), and full XZ (green panel) and YZ (red panel) projections. The level of co-localization is high based on Pearson's correlation coefficient (0.7-0.9, n=20). The highest level of co-localization is detected at the apical cortex.
- (c) Fluorescence pictures of Plin-26::VAB-10(ABD)::mCherry (red) and SPC-1::GFP (green): the panel shows the colocalization image for the most apical focal planes (top image), and full XZ (green panel) and YZ (red panel) projections. The level of co-localization is high based on Pearson's correlation coefficient (0.7-0.9, n=8). The co-localization is almost exclusively detected at the apical cortex.  
The gene lin-26 drives expression in the epidermis; VAB-10(ABD) corresponds to the two actin-binding domains (calponin homology) of the protein VAB-10. Scale bar, 10 μm.



**Supplementary Figure 4:** Actin filament continuity and orientation at three elongation stages

Actin filaments were visualised using a Pepid::Lifeact::GFP construct and characterised as outlined in Fig. 3a (the Pepid promoter corresponds to Pdpy-7).

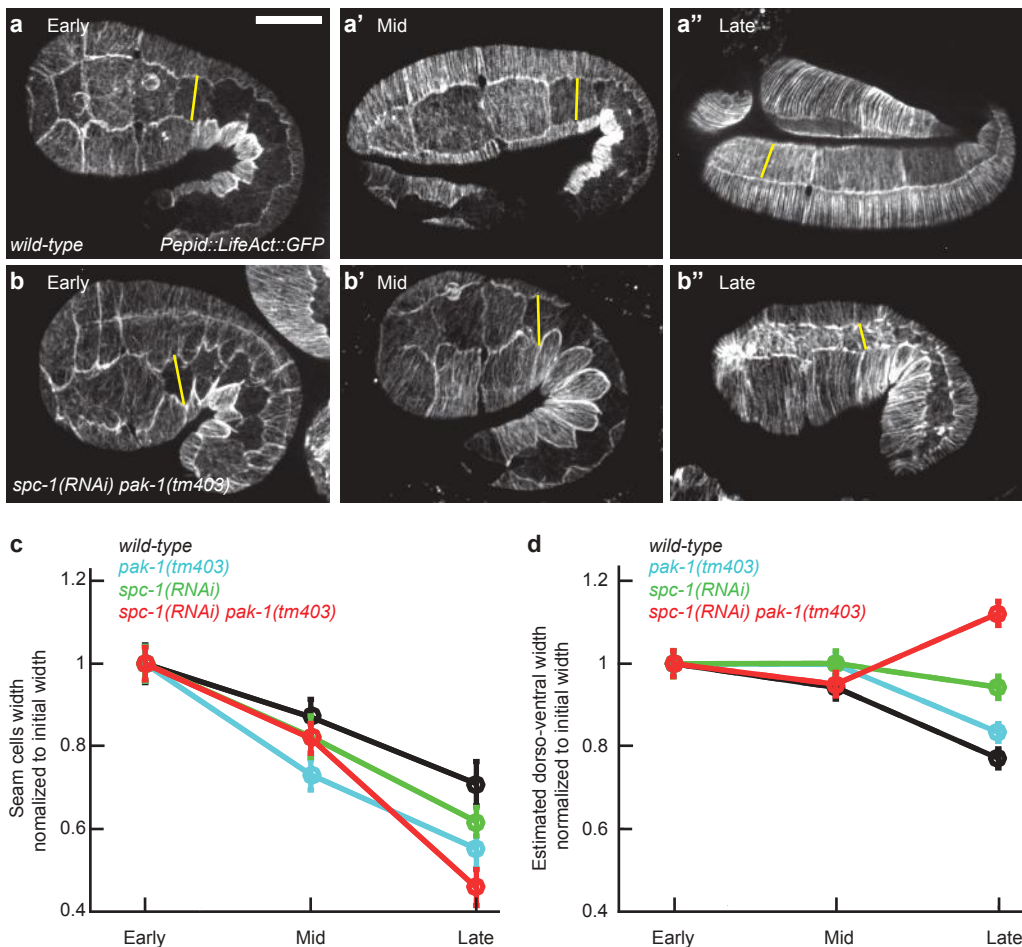
(a) Actin filament continuity. The graph represents the length (in pixels) along the circumferential axis of actin filaments in early, mid and late (corresponding to 1.7-fold, 2-fold and 3-fold equivalent stages in a wild-type embryo, respectively) embryos of wild-type (early n=12, mid n=19, late n=16), pak-1(tm403) (early n=16, mid n=21, late n=16), spc-1(RNAi) (early n=15, mid n=21, late n=20), and spc-1(RNAi) pak-1(tm403) (early n=12, mid n=17, late n=26) genotypes.

(b) Actin filament orientation based on Fast Fourier Transform

and binarisation. Wild type (early n=12, mid n=18, late n=14), pak-1(tm403) (early n=16, mid n=20, late n=16), spc-1(RNAi) (early n=14, mid n=18, late n=18), and pak-1(tm403) + spc-1(RNAi) (early n=12, mid n=18, late n=21).

Note that the characteristics of actin filaments in spc-1(RNAi) pak-1(tm403) embryos differ mostly at the equivalent of the two-fold stage when muscles become active. At earlier and later stages, spc-1(RNAi) embryos and spc-1(RNAi) pak-1(tm403) embryos become similar.

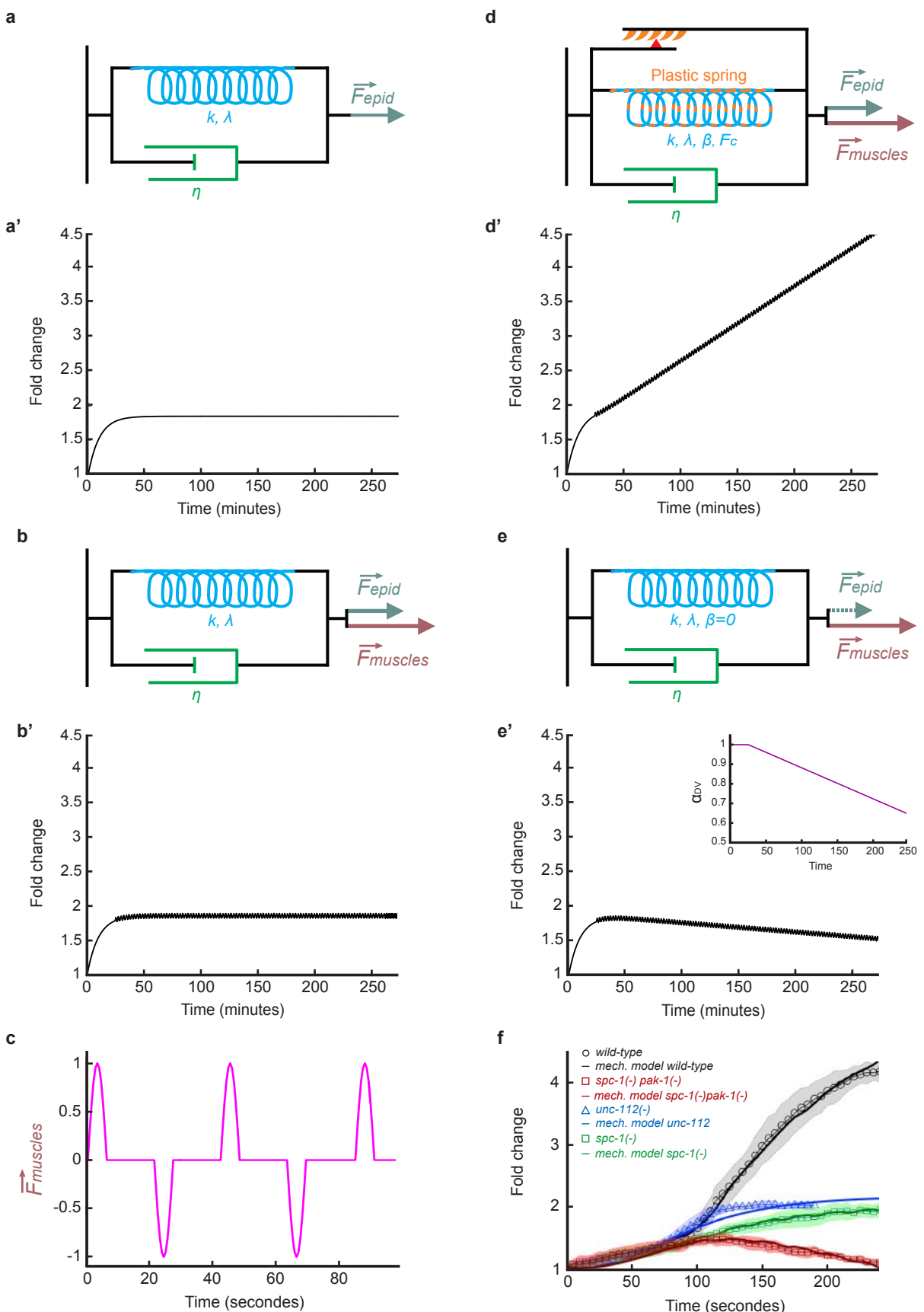
(c-f) Epidermal actin filaments visualized with the Pepid::Lifeact::GFP construct in wild-type (C), spc-1(RNAi) pak-1(tm403) (D) embryos (panels are from Fig. 3). \* $<0.05$ ; \*\* $<0.001$ ; \*\*\* $<0.0001$ ; ns, not significant.



**Supplementary Figure 5:** Change in embryo diameter during elongation

(a-b'') Fluorescence micrographs of embryos expressing the *Pepid::Lifeact::GFP* construct in the epidermis at three elongation stages early, middle and late (corresponding to 1.7-fold, 2-fold and 3-fold equivalent stages in a wild-type embryo, respectively) for wild-type (a-a'') and *spc-1(RNAi)* *pak-1(tm403)* embryos (b-b''); the *Pepid* promoter corresponds to *Pdpy-7*. The yellow lines correspond to the segments used to measure the dorso-ventral width of the V1 seam cell. (c) Quantification of the average V1 cell width normalized to the initial width during elongation in four genotypes. (d) Quantification of the average dorso-ventral width at the level of the V1 seam cell, which was calculated using the measured embryo length and V1 cell width, taking into consideration the conservation of the total embryo volume. Each point in panel (c) and (d) represents between 7 and 21 embryos; error bars are standard errors.

A notable feature of *spc-1(RNAi)* *pak-1(tm403)* embryos is that the circumferential dimension of the seam cells decreased much more than that of their DV cell, which most likely reflects the actin filament integrity defects combined with a Fseam force largely unchanged.



**Supplementary Figure 6:** Time-dependent length of a Kelvin-Voigt model in different conditions.

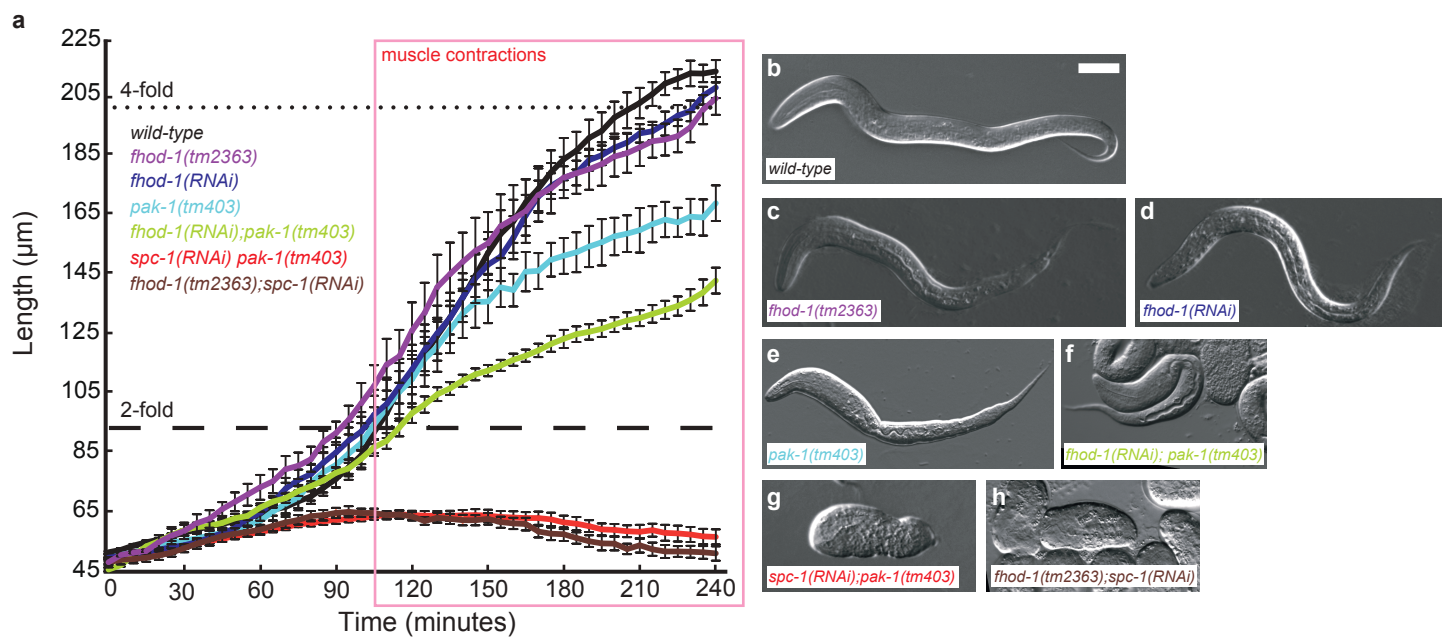
(a-a') A generic Kelvin-Voigt system subject to a constant force  $F_{epid}$  and its predicted elongation change using  $F_{epid}=0.85$  (A').

(b-b') A similar system subject to two forces,  $F_{epid}$  and an oscillating force  $F_{muscles}$  with the properties depicted in (E), and predicted elongation change using  $F_{epid}=0.85$  (B'). As the pulsatile force induces both compression and stretching (see Fig. S6), its net input on elongation is transient and the system oscillates around the maximal value reached without  $F_{muscles}$ .

(d-d') A Kelvin-Voigt system with mechanical plasticity introduced according to Eqs. (1,4-7), and predicted elongation change using  $F_{epid}=0.85$ ,  $\beta=0.10$  and  $F_c=0$  according to Eqs. (1,4-7). (e) A Kelvin-Voigt system in which the plasticity is defective ( $\beta=0$ ), and there is actin tearing according to Eq. (7) inducing a progressive reduction of  $F_{epid}$ , and predicted elongation change using  $F_{epid}=0.85$ , with an initial value of the passive component  $\alpha_{DV}(t=0)=1$  and the tearing factor  $\gamma=0.15$  (D').

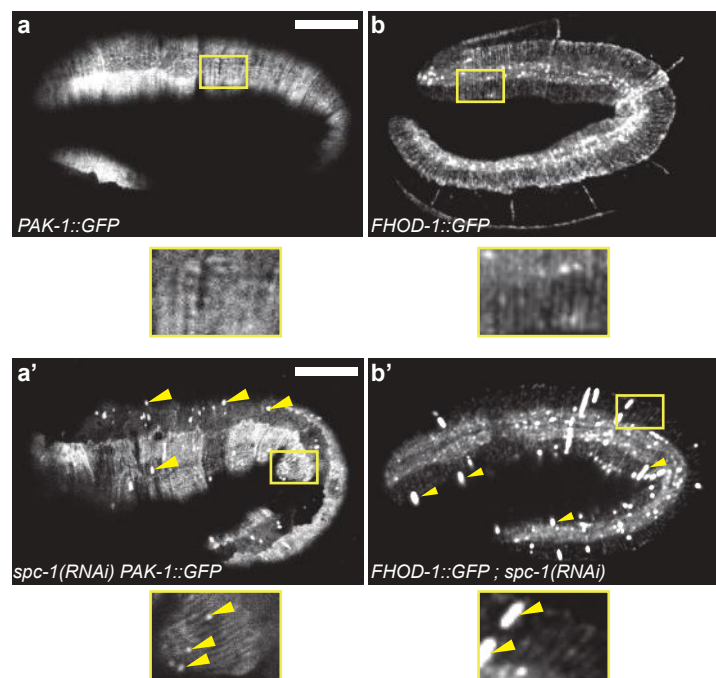
(e') Inset) Behavior of  $\alpha_{DV}$ .

(c) In all conditions  $F_{muscles}$  is a periodic function with positive and negative steps of duration of 6 seconds alternating with periods of null value of duration 15 seconds modulated by a cosine function. In (a-e') the elastic constant of the spring is  $k=1$ , the initial resting length has the value  $\lambda(t=0)=1$ , and the viscosity value is  $\eta=10$ . (f) Result of the fit for the following genotypes: wt, spc-1 pak-1, unc-112 and spc-1 according to Eqs. (1,4-7). The values of the parameters are specified in paragraphs 1.4, 1.5 and 1.6.



**Supplementary Figure 7:** Comparable retraction phenotypes after the combined loss of SPC-1 and PAK-1 or SPC-1 and FHOD-1

(a) Elongation curves of the single and double deficient embryos indicated on the left, (b-h) and corresponding terminal phenotypes at hatching: wild-type (n=5), *fhod-1(tm2363)* (n=6) *fhod-1(RNAi)* (n=7) *pak-1(tm403)* (n=5) *fhod-1(RNAi); pak1(tm403)* (n=7), *spc-1(RNAi)* *pak-1(tm403)* (n=8), *fhod-1(tm2363);spc-1(RNAi)* (n=9). Scale bar, 25  $\mu\text{m}$ .

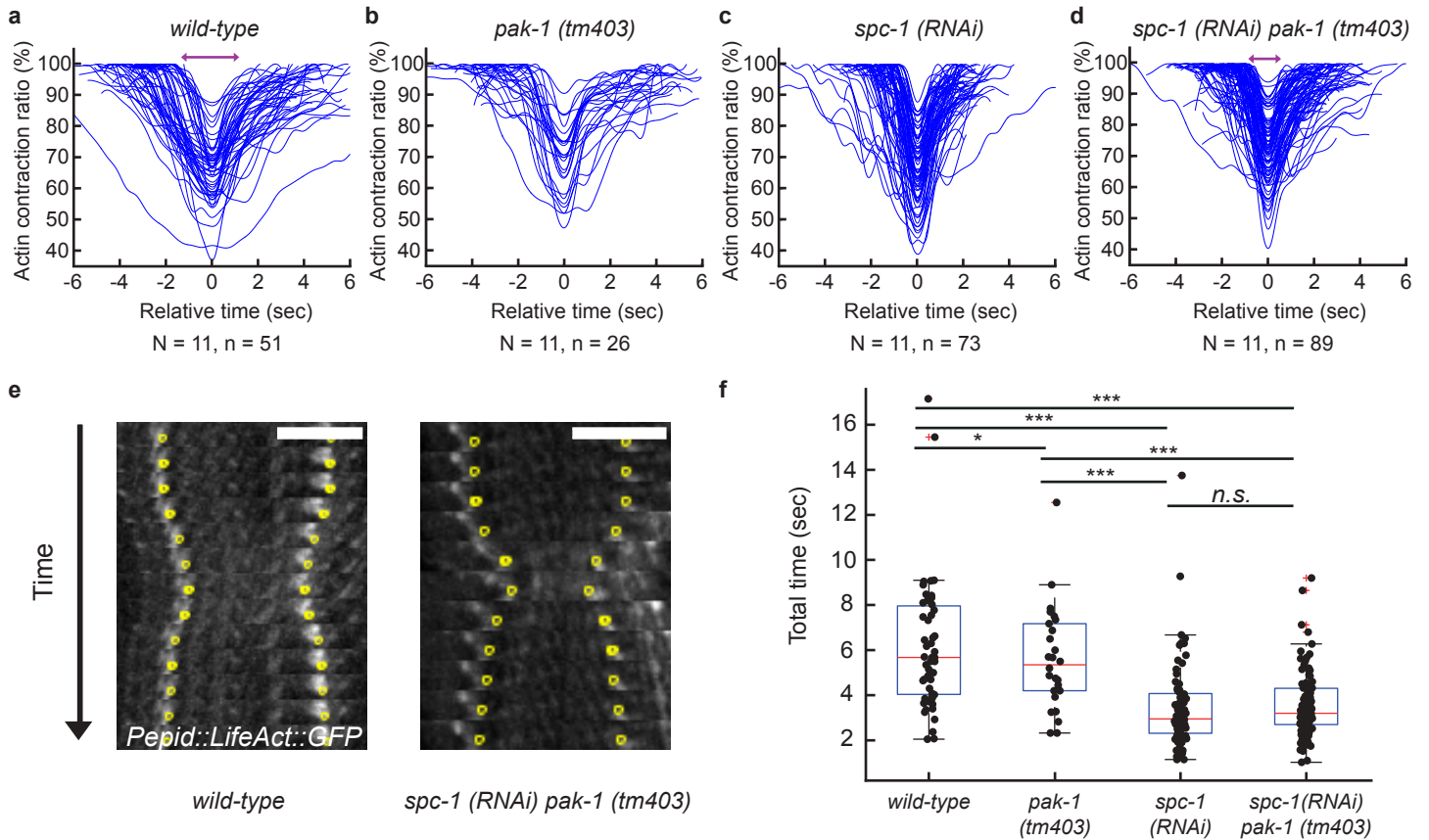


**Supplementary Figure 8:** PAK-1 and FHOD-1 form aggregates in *spc-1(RNAi)* loss of function.

(a-a') PAK-1::GFP localisation in wild-type and *spc-1(RNAi)* embryos. Yellow box, area enlarged below the panel.  
Note the punctae in SPC-1 deficient embryos.

(b-b') FHOD-1 localization in wild-type and *spc-1(RNAi)* embryos.

Note the aggregates (arrowheads). Note also that FHOD-1::GFP displayed a filamentous organization reminiscent of actin filaments.  
Scale bar: 10  $\mu$ m.



**Supplementary Figure 9:** Actin displacement ratio

(a-d) Individual displacement tracks of actin filaments visualized with a Pdpy-7::Lifeact::GFP marker specifically expressed in the epidermis of wild type (a), pak-1(tm403) (b), spc-1(RNAi) (c) and spc-1(RNAi) pak-1(tm403) (d) embryos at a stage equivalent to 2-fold in a wild-type embryo. Scale bar: 10  $\mu$ m.

(e) Typical kymographs of Pepid::GFP-labeled actin filaments in wild-type and spc-1(RNAi) pak-1(tm403) embryos from which the tracks in a-d were derived. Yellow dots correspond to landmarks for quantitative analysis.

(f) Quantification of the displacement duration in (N=embryo/ n=contraction): wild-type, N=11/n=51; pak-1(tm403), N=11/n=26; spc-1(RNAi), N=11/n=73; spc-1(RNAi) pak-1(tm403), N=11/n=89. \* $<0,05$ ; \*\* $<0,001$ ; \*\*\* $<0,0001$ ; ns, not significant.

<b>A</b>	Reproducible 50-100% enhanced defect* compared to wild-type
<b>B</b>	Reproducible 20-50% enhanced defect* compared to wild-type
<b>C</b>	Reproducible 5-20% enhanced defect* compared to wild-type

<b>Targeted gene</b>	<b>Function</b>	<b>Strength of interaction</b>
(III) <i>ani-1</i>	Anilin	A
(IV) <i>cap-1</i>	F-actin capping protein $\alpha$ subunit	A
(II) <i>cap-2</i>	$\beta$ subunit of actin capping protein	A
(V) <i>cdc-25.2</i>	Putative homolog of Cdc25 phosphatase	A
(II) <i>cdc-42</i>	RHO GTPase	A
(III) <i>dlc-1</i>	Dynein light chain	A
(IV) <i>epi-1</i>	Laminin $\alpha$ chain	A
(I) <i>hmp-2</i>	$\beta$ -catenin	A
(IV) <i>lam-1</i>	Laminin $\beta$	A
(I) <i>let-502</i>	Rho-binding Ser/Thr kinase	A
(III) <i>mlc-5</i>	Myosin II essential light chain ortholog	A
(I) <i>pfn-1</i>	Profilin	A
(V) <i>sma-1</i>	$\beta$ H-spectrin	A
(X) <i>spc-1</i>	$\alpha$ -spectrin	A
(I) <i>sur-6</i>	Regulatory subunit of serine/threonine protein phosphatase 2A	A
(X) <i>tni-1</i>	Troponin	A
(II) <i>dsh-2</i>	Dishevelled (Dsh) homolog	B
(I) <i>goa-1</i>	Ortholog of the heterotrimeric G protein $\alpha$ subunit Go	B
(I) <i>hmr-1</i>	Cadherin	B
(I) <i>kin-10</i>	Putative regulatory ( $\beta$ ) subunit of casein kinase II	B
(V) <i>mom-2</i>	Member of the Wnt family	B
(II) <i>mpk-2</i>	Mitogen activated protein (MAP) kinase	B
(I) <i>pfid-3</i>	Putative prefoldin, orthologous to human VBP1	B
(II) <i>aakg-5</i>	AMP kinase	C
(V) <i>arx-2</i>	Subunit of the actin related protein of the conserved Arp2/3 complex	C
(III) <i>arx-3</i>	Subunit of the actin related protein of the conserved Arp2/3 complex	C
(I) <i>bub-1</i>	Serine/threonine kinase	C
(V) <i>chk-1</i>	CHK1-like serine threonine protein kinase	C
(I) <i>chp-1</i>	Protein containing two CHORD domains	C
(I) <i>csnk-1</i>	Ortholog of human CSNK1G3, CSNK1G1 and CSNK1G2	C
(II) <i>ect-2</i>	Putative RHO guanine nucleotide exchange factor (RhoGEF)	C
(I) <i>ekl-1</i>	Ortholog of members of the human TDRD	C
(IV) <i>fln-1</i>	Filamin	C
(X) <i>ifa-3</i>	Intermediate filament protein	C
(III) <i>klp-19</i>	Plus-end-directed microtubule motor protein	C
(III) <i>lit-1</i>	Serine threonine protein kinase	C
(I) <i>mei-2</i>	Novel protein containing a region similar to the p80-targeting subunit of katanin	C
(V) <i>mrck-1</i>	Serine/threonine-protein kinase	C
(III) <i>par-2</i>	Protein containing a C3HC4-type RING-finger	C
(III) <i>pfid-5</i>	Putative prefoldin 5 subunit	C
(I) <i>sys-1</i>	Novel protein that contains three divergent armadillo repeats	C
(II) <i>spv-1</i>	Ortholog of human GMIP	C
(I) <i>tbcd-1</i>	Putative $\beta$ -tubulin folding cofactor D	C
(I) <i>usp-5</i>	Ortholog of human USP5 and USP13	C
(II) <i>Y19D2B.1</i>	Structural constituent of cytoskeleton	C

\* Defect refers to lethality and body morphology defects

Table S1

No enhanced defect\* compared to wild-type

(I) <i>afd-1</i>	(II) <i>aak-1</i>	(III) <i>abce-1</i>	(IV) <i>arp-11</i>	(V) <i>air-1</i>	(X) <i>aakb-1</i>
<i>arx-7</i>	<i>arp-1</i>	<i>abi-1</i>	<i>ced-5</i>	<i>cct-7</i>	<i>aakg-2</i>
<i>aspm-1</i>	<i>C27H5.4</i>	<i>arf-1.2</i>	<i>dli-1</i>	<i>F14H3.12</i>	<i>abl-1</i>
<i>chs-1</i>	<i>cacn-1</i>	<i>cct-5</i>	<i>dnc-1</i>	<i>gck-2</i>	<i>dyn-1</i>
<i>col-53</i>	<i>cal-2</i>	<i>cct-6</i>	<i>dyci-1</i>	<i>knl-3</i>	<i>efn-3</i>
<i>cpn-1</i>	<i>ccm-3</i>	<i>cls-1</i>	<i>eps-8</i>	<i>mig-6</i>	<i>F20B6.1</i>
<i>cutl-13</i>	<i>cct-1</i>	<i>cls-2</i>	<i>frk-1</i>	<i>noca-1</i>	<i>frm-9</i>
<i>dhc-1</i>	<i>cct-2</i>	<i>col-94</i>	<i>gex-2</i>	<i>pak-2</i>	<i>hpk-1</i>
<i>dlc-6</i>	<i>cct-4</i>	<i>col-97</i>	<i>gex-3</i>	<i>par-1</i>	<i>ifa-2</i>
<i>eak-6</i>	<i>cdc-25.4</i>	<i>cra-1</i>	<i>klp-10</i>	<i>rbx-1</i>	<i>kin-29</i>
<i>egg-5</i>	<i>cpn-2</i>	<i>cyk-4</i>	<i>klp-11</i>	<i>spas-1</i>	<i>lam-2</i>
<i>egg-6</i>	<i>dep-1</i>	<i>daf-4</i>	<i>klp-5</i>	<i>sun-1</i>	<i>lin-18</i>
<i>ekl-4</i>	<i>ebp-2</i>	<i>fem-2</i>	<i>let-60</i>	<i>syx-5</i>	<i>lpr-3</i>
<i>erm-1</i>	<i>eff-1</i>	<i>frm-2</i>	<i>let-92</i>	<i>unc-112</i>	<i>nck-1</i>
<i>fhod-1</i>	<i>egg-3</i>	<i>gei-4</i>	<i>M116.5</i>	<i>unc-70</i>	<i>pak-1</i>
<i>gei-17</i>	<i>evl-20</i>	<i>gop-3</i>	<i>nsp-1</i>		<i>pfn-2</i>
<i>gfi-2</i>	<i>F59A6.5</i>	<i>ina-1</i>	<i>par-5</i>		<i>pfn-3</i>
<i>gsa-1</i>	<i>frm-5.2</i>	<i>inft-1</i>	<i>pdf-1</i>		<i>pqn-34</i>
<i>gsk-3</i>	<i>glb-12</i>	<i>kin-18</i>	<i>pld-1</i>		<i>unc-97</i>
<i>gsp-3</i>	<i>gpb-1</i>	<i>klp-6</i>	<i>pmk-2</i>		
<i>gsp-4</i>	<i>klp-1 / unc-104</i>	<i>klp-7</i>	<i>pmk-3</i>		
<i>kca-1</i>	<i>klp-17</i>	<i>let-805</i>	<i>ptp-4</i>		
<i>lim-9</i>	<i>let-268</i>	<i>mpk-1</i>	<i>rac-1 / ced-10</i>		
<i>mel-26</i>	<i>lrr-1</i>	<i>mtrm-3</i>	<i>rack-1</i>		
<i>mfap-1</i>	<i>max-2</i>	<i>nfm-1</i>	<i>unc-33</i>		
<i>mom-5</i>	<i>mel-11</i>	<i>pef-1</i>	<i>wsp-1</i>		
<i>nab-1</i>	<i>mig-5</i>	<i>plk-1</i>	<i>zen-4</i>		
<i>ned-8</i>	<i>mlt-8</i>	<i>pph-6</i>			
<i>nkb-1</i>	<i>nsy-1</i>	<i>ptp-1</i>			
<i>nmy-2</i>	<i>pdf-2</i>	<i>pxl-1</i>			
<i>npp-4</i>	<i>pink-1</i>	<i>rfl-1</i>			
<i>ocrl-1</i>	<i>pir-1</i>	<i>tbb-2</i>			
<i>pes-7</i>	<i>ptc-3</i>	<i>ten-1</i>			
<i>pdf-6</i>	<i>ptp-2</i>	<i>tlk-1</i>			
<i>ppk-1</i>	<i>ptp-3</i>	<i>trd-1</i>			
<i>rga-2</i>	<i>saps-1</i>	<i>unc-116</i>			
<i>rsa-1</i>	<i>scpl-2</i>	<i>wrm-1</i>			
<i>smgl-1</i>	<i>sds-22</i>				
<i>spd-1</i>	<i>spdl-1</i>				
<i>tba-2</i>	<i>tac-1</i>				
<i>ttx-7</i>	<i>tba-4</i>				
<i>unc-35</i>	<i>unc-52</i>				
<i>unc-59</i>	<i>vab-19</i>				
<i>unc-73</i>	<i>vab-9</i>				
<i>unc-73</i>	<i>vhp-1</i>				
<i>unc-94</i>	<i>vps-11</i>				
<i>vab-10</i>	<i>vps-32</i>				
<i>viln-1</i>	<i>W0761.1</i>				
<i>vps-20</i>	<i>zyg-9</i>				
<i>wve-1</i>					

**Global PBS /Predicted Biological Score/**  
categories computed and established by Hybrigenics, to assess the interaction reliability

A	Very high confidence in the interaction
B	High confidence in the interaction
C	Good confidence in the interaction
D	Moderate confidence in the interaction <i>/either due to false-positive interactions or due to interactions that are hardly detectable by the Y2H technique/</i>

**Strongest candidates**  
/ Prey library: *C. elegans embryo* /

Primary Yeast Two Hybrid Screen		
<i>/ Bait: CePAK-1 N-terminal amino acids: 1-294 /</i>		
Interactor candidate	Protein function	Global PBS
SPC-1	α-spectrin	A
F47B10.1	β-chain succinyl-co-A ligase	A
CHW-1	RhoU homolog	A
GCK-1	STE20-family kinase	A
NCK-1	NCK adaptor	A
PIX-1 *	ARHGEF7 homolog β-Pix	A
CDC-42 *	Small GTPase	A
PAK-1 *	P21-activated Ser/Tre kinase (multiple hits through kinase domain)	A
CED-10 *	Rac-1 / Small GTPase	B
POD-2	Predicted acetyl-coA carboxylase	B
Y39E4A.3	Transketolase	B
EEL-1	HECT-ubiquitin ligase	C
NPP-21	Nuclear pore protein	C
TAG-143	Transcription factor	C
UNC-44	Ankyrin	D
HIPR-1	SLA2 and Hip related	D
T05C1.4	Conserved calmodulin-binding TFs	D
Y53F4B.13	RNA methyltransferase	D
PTP-3	LAR-like receptor tyr-protein phosphatase	D
COGC-6	Conserved Oligomeric Golgi (COG) Component	D
DAF-21	Hsp90 molecular chaperone family member	D
GCK-1 variant	STE20-family kinase	D

Secondary Yeast Two Hybrid Screen		
<i>/ Bait I: CeSPC-1 SR8-10(aa:796-1243) /</i>		
<i>/ Bait II: CeSPC-1 SH3 (aa:986-1041) /</i>		
<i>/ common hits using Bait I and Bait II /</i>		
Interactor candidate	Protein function	Global PBS
PAK-1	p21-activated Kinase	A
LIM-8	LIM domain muscle component	A
F44.E2.3	ARGLU1 ortholog	A
CSN-5	COP9-subunit ortholog, E3 ubiquitin ligase interactor	A
DEB-1	Vinculin	A
Dnaj	DNAJ/ZRF1/MPP11 ortholog; ribosome-associated chaperone	B
CYLD-1	Human CYLD1 ortholog, NF-κB signalling interactor	B
VAB-3 / VAR-1	Homeodomain protein PAX6 ortholog	B
GRL-4	Hedgehog-like protein	C
UNC-34	Enabled/VASP homolog	C
T04F8.6	Human ninein and ninein-like (GSK3B interactor) ortholog	D
ALR-1	Human ARX(aristaless) ortholog homeodomain transcription factor	D
ATN-1	α-actinin homolog	D
MMCM-1	Methylmalonyl-CoA mutase	D
UNC-70	β <sub>G</sub> -spectrin	D
VAB-10	Spectraplakin	D
F26A10.2	Zinc-finger containing protein (required for germ line maintenance and locomotion)	D
F43C1.1	Human PHLPP1&PHLPP2 (PH domain&leucine-rich repeat Protein Phosphatase) ortholog	D
ALP-1	Enigma family member ALP (α-actinin associated LIM Protein) ortholog; required for actin anchorage	D
CIT-1.2	Cyclin T ortholog, embryonic transcriptional regulator	D
FLH-1	FLYWCH zinc finger transcription factor homolog	D
SHW-1	Human KCNC3 voltage-gated Shaw family potassium channel ortholog	D

\* Positive controls (PAK-1 itself + its known interactors)

<b>A</b>	Shorter compared to <i>spc-1(-)</i>
<b>B</b>	Not shorter than <i>spc-1(-)</i>

<i>Targeted gene</i>	<i>Function</i>	<i>Strength of interaction</i>
(I) <i>fhod-1</i>	<b>Formin</b>	<b>A</b>
(I) <i>hmr-1</i>	<b>Cadherin</b>	<b>A</b>
(I) <i>hmp-2</i>	<b>β-catenin</b>	<b>A</b>
(II) <i>cdc-42</i>	<b>RHO GTPase</b>	<b>A</b>
(II) <i>spd-1</i>	<b>Coiled-coil protein</b>	<b>A</b>
(III) <i>vps-11</i>	<b>Ortholog of human VPS11</b>	<b>A</b>
(III) <i>mtm-3</i>	<b>Myotubularin lipid phosphatase</b>	<b>A</b>
(III) <i>mlc-5</i>	<b>Myosin II essential light chain ortholog</b>	<b>A</b>
(IV) <i>dnc-1</i>	<b>Ortholog of the dynactin complex subunit p150/GLUED/DCTN1</b>	<b>A</b>
(IV) <i>epi-1</i>	<b>Laminin α chain</b>	<b>A</b>
(I) <i>goa-1</i>	<b>Ortholog of the heterotrimeric G protein α subunit Go</b>	<b>B</b>
(I) <i>kin-10</i>	<b>Putative regulatory (β) subunit of casein kinase II</b>	<b>B</b>
(I) <i>mec-8</i>	<b>mRNA processing factor</b>	<b>B</b>
(I) <i>nmy-2</i>	<b>Non-muscle myosin II</b>	<b>B</b>
(I) <i>unc-94</i>	<b>Tropomodulin</b>	<b>B</b>
(II) <i>cap-2</i>	<b>β subunit of actin capping protein</b>	<b>B</b>
(II) <i>evl-20</i>	<b>Ortholog of human ADP-ribosylation factor-like protein 2</b>	<b>B</b>
(II) <i>spv-1</i>	<b>Ortholog of human GMIP</b>	<b>B</b>
(II) <i>unc-52</i>	<b>Perlecan</b>	<b>B</b>
(III) <i>klp-7</i>	<b>Ortholog of human KIF2A, 2B and 2C</b>	<b>B</b>
(III) <i>mup-4</i>	<b>Transmembrane protein</b>	<b>B</b>
(IV) <i>cap-1</i>	<b>F-actin capping protein α subunit</b>	<b>B</b>
(IV) <i>eps-8</i>	<b>Cell signaling adaptor protein</b>	<b>B</b>
(IV) <i>frk-1</i>	<b>Non-receptor tyrosine kinase</b>	<b>B</b>
(IV) <i>unc-33</i>	<b>Conserved member of the CRMP/TOAD/Ulip/DRP family</b>	<b>B</b>

**Table S3**

Name	<i>Genotype</i>
<b>DM3409</b>	<i>mnDp33 (X;IV)/+ IV.; spc-1(ra409) X.</i>
<b>DWP10</b>	<i>fhod-1(tm2363) I.; qals8001 [unc-119(+)] fhod-1::gfp]</i>
<b>ML1694</b>	<i>pix-1(gk416)X.</i>
<b>ML1725</b>	<i>mcEX567 [spc-1::GFP, myo-2p::mcherry]</i>
<b>ML1822</b>	<i>sma-1(ru18)V.; pak-1 (tm403)X.</i>
<b>ML1943</b>	<i>mcIs55[pak-1::GFP;pRF4]</i>
<b>ML1911</b>	<i>git-1(tm1962)X.</i>
<b>ML2113</b>	<i>mcIs67 [dpy7p::LifeAct::GFP; unc-119(+)] V.; stls10088[hlh-1::his-24::mCherry, unc-119(+)]</i>
<b>ML2129</b>	<i>pak-1(tm403) X.</i>
<b>ML2200</b>	<i>pak-1(tm403) X.; mcIs67 [dpy7p::LifeAct::GFP; unc-119(+)] V; stls10088[hlh-1::his-24::mCherry, unc-119(+)]</i>
<b>ML2419</b>	<i>mcEx915[ppak-1::pak-1::mkate;pR4(rol);pBSK]</i>
<b>ML2428</b>	<i>sma-1(ru18)V.</i>
<b>ML2436</b>	<i>spc-1(ra409) X.; mcEx636 [spc-1p::spc-1::GFP]</i>
<b>ML2446</b>	<i>pak-1(tm403) X.; spc-1(ra409) X.; mcEx636 [spc-1p::spc-1::GFP]</i>
<b>ML2465</b>	<i>mcIs91[linc26p::ABD::mkate; myo-2p::mcherry]</i>
<b>ML2684</b>	<i>mcEx1008 [fhod-1 ΔFH2/DAD]</i>
<b>ML2688</b>	<i>pak-1(tm403) X.; mcEx1009 [fhod-1 ΔFH2/DAD]</i>
<b>ML2853</b>	<i>pak-1(tm403) X.; mcEx1002 [fhod-1 ΔFH1/FH2/DAD]</i>
<b>ML2854</b>	<i>pak-1(tm403) X.; mcEx1003 [fhod-1 ΔDAD]</i>
<b>ML2855</b>	<i>pak-1(tm403) X.; mcEx1004 [fhod-1 full length]</i>
<b>ML2856</b>	<i>mcEx1005 [fhod-1 ΔFH1/FH2/DAD]</i>
<b>ML2857</b>	<i>mcEx1006 [fhod-1 ΔDAD]</i>
<b>ML2858</b>	<i>mcEx1007 [fhod-1 full length]</i>
<b>N2</b>	<i>Bristol</i>
<b>XA8001</b>	<i>fhod-1(tm2363) I.</i>

**Table S4**